

# Exciton-polariton condensate in the van der Waals magnet CrSBr

Bo Han<sup>1,7</sup>, Hangyong Shan<sup>1,7</sup>, Kok Wee Song<sup>2</sup>, Lukas Lackner<sup>1</sup>, Martin Esmann<sup>1</sup>, Vita Solovyeva<sup>1</sup>, Falk Eilenberger<sup>3,4,5</sup>, Jakub Regner<sup>6</sup>, Zdeněk Sofer<sup>6</sup>, Oleksandr Kyriienko<sup>2</sup> and Christian Schneider<sup>1,\*</sup>

<sup>1</sup>*Institute of Physics, Faculty V, Carl von Ossietzky University Oldenburg, 26129 Oldenburg, Germany.*

<sup>2</sup>*Department of Physics and Astronomy, University of Exeter, Exeter EX4 4QL, United Kingdom.*

<sup>3</sup>*Institute of Applied Physics, Abbe Center of Photonics, Friedrich Schiller Universität Jena, 07745 Jena, Germany.*

<sup>4</sup>*Fraunhofer-Institute for Applied Optics and Precision Engineering IOF, 07745 Jena, Germany.*

<sup>5</sup>*Max Planck School of Photonics, 07745 Jena, Germany.*

<sup>6</sup>*Department of Inorganic Chemistry, Faculty of Chemical Technology, University of Chemistry and Technology Prague, Technická 5, Prague 6, 16628, Czech Republic.*

<sup>7</sup>*These authors contributed equally.*

\* *E-mails: christian.schneider@uni-oldenburg.de*

**Van der Waals magnets are an emergent material class of paramount interest for fundamental studies in coupling light with matter excitations, which are uniquely linked to their underlying magnetic properties. Among these materials, the magnetic semiconductor CrSBr is possibly a first playground where we can study simultaneously the interaction of photons, magnons, and excitons at the quantum level. Here we demonstrate a coherent macroscopic quantum phase, the bosonic condensation of exciton-polaritons, which emerges in a CrSBr flake embedded in a fully tunable cryogenic open optical cavity. The Bose condensate is characterized by a highly non-linear threshold-like behavior, and coherence manifests distinctly via its first and second order quantum coherence. We find that the condensate's non-linearity is highly susceptible to the magnetic order in CrSBr, and encounters a sign change depending on the antiferro- and ferromagnetic ordering. Our findings open a route towards magnetically controllable quantum fluids of light, and optomagnonic devices where spin magnetism is coupled to on-chip Bose-Einstein condensates.**

## Introduction

The emerging class of van der Waals magnets offers unprecedented opportunities to interface magnetism with light in structures that are controllable at the atomic limit<sup>1</sup>. Among these materials, CrSBr crystals, which are magnetic van der Waals semiconductors and stable under ambient conditions, are of specific interest<sup>2</sup>. In these materials, excitons are prominent down to the monolayer limit<sup>3,4</sup>, and dictate the optical response over a large temperature range<sup>5-8</sup>. From the few-layer thin

film to the bulk, below the Néel temperature of 132 K, the magnetic ground state is represented by an A-type interlayer antiferromagnetic (AFM) order<sup>3,9,10</sup> (Fig. 1b). In this magnetic phase, excitons are strongly confined within the individual layer due to spin-forbidden interlayer charge transfer<sup>3,11</sup>.

The magnetic order can be controlled by strain and hydrostatic pressure<sup>12,13</sup>, electrostatic doping<sup>4</sup> and in externally applied magnetic fields. Out-of-plane magnetic fields can force the system into a parallel spin configuration (staggered ferromagnetic (FM) order, see Fig. 1b). The exciton energy changes drastically with the interlayer hybridization<sup>3,6</sup>, and thus represents a direct optical read-out channel for the magnetic order. In presence of external magnetic fields, the excitonic landscape is further modulated by coherent magnons<sup>14</sup>, which emerge in the system and have recently been observed in pump-probe studies.<sup>6,7,15,16</sup> These phenomena attest strong interplay between the magnetic-electronic-optical properties in CrSBr. The interplay between magnetic order and the light-matter coupling in optical cavities, to date, has been explored less intensely. First reports have verified the emergence of strongly coupled exciton-polaritons in bare CrSBr slabs<sup>6</sup> and those embedded in external optical cavities<sup>6,17-19</sup>, and highlighted the magnetic response of the hybrid light-matter quasiparticles.

However, these magneto-optical studies were performed in the linear regime, where exciton correlations can be widely neglected in the polariton gas. In turn, a major appeal arises to explore high-density regimes of exciton-polaritons in 2D magnets, as condensate phases that interact with the underlying magnetic order of the

crystal remain elusive thus far. Here, we use a cryogenic tunable optical microcavity with a high quality factor to acquire the necessary in-situ control of the light-matter composition of CrSBr exciton-polaritons for the transition to the non-linear regime of polariton condensation. The emergent exciton-polariton condensate is evidenced by the threshold-like emission output, and distinct via its first and second order coherence. The interplay of the condensate with the magnetic order yields an intriguing new kind of tunable polariton non-linearity that is driven by the excitation of incoherent magnons. We demonstrate that polaritonic engineering is a powerful tool to probe the magnetic correlations and magnetically controlled quantum phases in CrSBr.

### Tunable magneto-exciton-polaritons of CrSBr in an open-access optical cavity

For our study, we utilize a thin CrSBr flake, which we prepare via exfoliation and subsequent dry transfer on a SiO<sub>2</sub>/TiO<sub>2</sub> distributed Bragg reflector (DBR). The thickness of the slab is determined as  $312 \pm 2$  nm via atomic force microscopy measurements (Supplementary Fig. S1d). Owing to the drastic dielectric contrast between the CrSBr crystal and the surrounding medium, for instance the substrate materials and vacuum, the crystal by itself already composes a Fabry-Pérot cavity, contrasting the situation of nanometer thin flakes or bulk crystals. The light-matter coupling strength of excitons in CrSBr was found to be sufficient to support the emergence of self-hybridized exciton-polaritons<sup>6,17</sup>, while the energy of these polaritonic resonances depend sensibly on the exact thickness of the CrSBr crystal. The optical transitions subject to our study thus need to be analyzed in a polaritonic picture.

The photoluminescence (PL) spectrum of our flake at 3.5 K features six self-hybridized polariton peaks that are labelled P<sub>1</sub>-P<sub>6</sub> (Fig. 1c), which are consistent with the reflection spectrum of a 318 nm thick flake placed on a DBR, simulated by the transfer matrix method (see experimental and simulation details in Methods). Further, direct evidence of the polaritonic nature of these peaks is reflected by their magnetic field response (left panel of Fig 1e): While all peaks sensibly react to an external out-of-plane magnetic field via a strong energy redshift, quantitatively, this shift depends critically on the peak energy. Indeed, P<sub>6</sub>, the energetically lowest self-hybridized polariton, features the smallest magnetic field shift, while the shift of the higher energy polaritons scales with their excitonic admixture that

is characterized by the excitonic Hopfield coefficient<sup>6,20</sup> (see Supplementary Eq. S10 and Fig. S2). The -13.3 meV magnetic shift of the P<sub>6</sub> mode corresponds to an excitonic Hopfield coefficient:  $|X|^2 = 0.76$  (see Supplementary note 3).

Active control of the system resonances is acquired by introducing a highly reflective top DBR, as depicted in Fig. 1a. (see supplementary Figs. S1a,b for details of the top mirror). The schematics capture the essence of the resulting tunable open-access cavity structure. In this setting, the gap between the top DBR and the CrSBr crystal is tunable via a DC voltage applied to the piezo nanopositioning stage. The concave-shaped DBR on the top mesa confines Laguerre-Gaussian modes of varying transversal mode order (up to five within a longitudinal mode order). These discretized zero-dimensional modes<sup>21</sup> have complex spatial profiles in real-space or momentum-space that have been explored via tomographic measurements<sup>22,23</sup>, and their theoretical quality factors (Q-factors) are estimated to exceed 5000 (see Supplementary Note 1). The energetically lowest transverse mode has a Gaussian-shaped profile, matching the Gaussian laser excitation beam used in our measurements, so that the PL intensity emitted through this mode is maximized and we only focus on the lowest transversal cavity modes in this work.

Figure 1d presents PL spectra as a function of the cavity detuning voltage, which was applied to tune the cavity (A maximum voltage of 60 V corresponds to  $\sim 0.6$   $\mu\text{m}$  of travel). We notice various sets of anti-crossings for each transverse cavity mode, which develop around the self-hybridized polaritons as we spectrally tune these discretized open-cavity resonances. This peculiar behavior is a clear signature of new exciton-polariton states, which hybridize the external high Q cavity modes with the self-hybridized polaritons in the CrSBr slab. The PL emission from the tunable cavity polaritonic modes is dominated by the lower polariton branch (LPB) and five middle polariton branches (MPBs) that have reduced intensity. We also observe spectral features of the upper polariton branch (UPB) that was not found in previous works<sup>6,17</sup>.

This strong coupling cascade can be approximated by an extended coupled oscillator model, considering six independent self-hybridized polariton states (P<sub>1</sub>-P<sub>6</sub>) and the Gaussian transversal modes (C<sub>1</sub>-C<sub>3</sub>) from three consecutive longitudinal mode orders (see the coupling matrix in Methods). More than one cavity mode

participate in the strong coupling and consequently bend the new polariton energies even above (and below) the  $P_6$  self-hybridized polariton state above 55 V (and below 10 V). As a result, the dispersion of the MPB connects directly to the LPB via the transversal modes of the same symmetry but different longitudinal mode orders. This phenomena can also be seen more clearly from the power-dependent PL measurements of the cavity scan (Supplementary Fig. S7). Diagonalizing the  $9 \times 9$  matrix gives us the eigenvalues of nine new exciton-polariton modes at different cavity detuning voltages (see Methods). The maximum coupling strength of  $V_6 = 33$  meV corresponds to the strong coupling of the cavity modes to  $P_6$ . This result is in contrast to the previously reported ultra-strong coupling regime of CrSBr excitons in a closed cavity structure<sup>17</sup>, since our polaritons arise from the resonant coupling of the self-hybridized polaritons with the external open cavity resonances.

Exciton-polaritons are bosonic quasi-particles, whose magnetic response arise from the excitonic component<sup>24</sup>. The out-of-plane magnetic field cants the electron spins away from the A-type anti-ferromagnetism in CrSBr, and the net magnetization of the crystal saturates as a forced ferromagnetic-like order at  $B_{\text{sat}} \sim 2$  T (Fig. 1b). As a result, the spin-allowed interlayer charge transfers take place<sup>11</sup>, and the exciton wave-function expands into the neighboring sheets. Thus, the energy of the excitons, and consequently, the emergent polaritons encounter a spectral redshift as a result of the admixture of more spin-parallel bands<sup>3,11</sup>. Similar to the spectral shift of the intrinsic self-hybridized polaritons, a magnetic response occurs for all of the new polariton modes in our open cavity (right panels of Fig. 1e). Notably, the amplitude of the magneto-polariton energy shifts depends sensibly on the in-situ adjustable detuning, which manifest the explicit Hopfield physics of the exciton-polaritons. This is most instructively reflected by the LPB that remains almost fully insensitive to the external B-field at 20 V (higher photonic regime, see Supplementary Fig. S2), and develops a considerable magnetic field shift at 50 V (higher excitonic regime), which is comparable to the energy shift of the self-hybridized  $P_6$  mode.

### Magnetic-phase dependent polaritonic non-linearity

Being bosonic quasi-particles, exciton-polaritons can undergo a phase transition into a coherent state at elevated density, while maintaining the inherent non-linear character of the excitons and retaining the fingerprints of specific magnetic order. As an exemplary demonstration

of such a formation of a coherent macroscopic quantum state, we probe our system at 0 T (AFM order) as well as 3 T (forced FM order) via density dependent measurements. The coupling strengths of the self-hybridized polaritons are nearly invariant to the applied magnetic field (Supplementary note 2 and Fig. S4a,b), consistent with previous magneto-optics measurements of a much thinner 7-layer CrSBr placed on a photonic crystal cavity<sup>18</sup>. Similar detuning conditions (44 V, 0 T and 38 V, 3 T) are chosen to warrant comparability between the magnetic-order contrasting experiments (Supplementary Fig. S4). We drive our system with off-resonant 725 nm laser pulses with 200 fs temporal pulse duration and 76 MHz repetition rate (see Methods). The maximum fluence energy is up to 0.66 nJ per pulse, corresponding to a time-averaged pump power of 50 mW for a free-space beam with diameter  $\sim 1$  mm.

Figures 2a,b depict the power dependent evolution of the discrete modes in the LPBs and the MPBs. Both sets of measurements feature qualitative similarities: the LPB modes of lowest energy progressively gain intensity, and eventually experience a pronounced blue-shift at pump powers above 33 mW, whereas the MPBs deplete in population in the high density regime, which is a clear signature of the effect of Bosonic final state stimulation. (A clear additional demonstration of this effect for various detunings is shown in Supplementary Fig. S7).

Both, the experimental data recorded at 0 T and 3 T reveal a clear superlinear increase in emission intensity over a large power range of 15-35 mW (Figs. 2c,f). This threshold-like behavior is accompanied by a reduction of the Lorentzian part of the emission lineshape, whereas a Gaussian contribution that arises from fast vibrational fluctuations of the cavity mode evolves in an opposite trend (Figs. 2d,g), probably due to the thermal excitation of the open cavity. At largest pump powers above 33 mW, the full width at half maximum (FWHM) strongly increases, which we assign to the pronounced density fluctuations in the LPB states, which is in a good agreement with earlier reports on polariton condensates driven with ultrashort laser pulses<sup>25-27</sup>. Indeed, in this regime, also the emission intensity in the ground state experiences a drop, which further supports our interpretation<sup>28</sup>.

For the maximum pump. power of 50 mW, we estimate the exciton density to be  $d_X^{50mW} = 4.54 \times 10^{11} \text{ cm}^{-2}$  in each layer of our CrSBr flake (see details in Supplementary note 4), which is well below the Mott

density on the order of  $10^{13} \text{ cm}^{-2}$  in a transition metal dichalcogenide monolayer<sup>29,30</sup>. Although  $d_X^{50mW}$  is on the same order of the Mott density in conventional III-V and II-VI semiconductor quantum wells, we expect the Mott density in a CrSBr layer is at least one order of magnitude higher, because the effective Bohr radius of excitons in CrSBr is much smaller<sup>31-33</sup>. Therefore, we suppose our system has not reached the Mott transition even for the maximum pump power applied (see detailed discussion in Supplementary note 4).

For both magnetic orders, the optical resonance displays two distinct regimes: Up to pump powers around 33 mW, the spectral shifts develop linearly with the pump power, and have modest values of a few meV. In addition, we capture a super-imposed redshift feature of the LPB for pump powers below 20 mW in the experiments (Supplementary Fig. S3 and S4d,e,h,i), which we attribute to a slight thermal expansion of our open cavity in combination with the interaction between the excitons and incoherent magnons. We can correct accurately the artificial redshift of the cavity modes caused by the thermal expansion, by referencing for purely photonic resonances (see Supplementary note 3).

Figures 2e,h show the polaritonic energy shifts of the lowest LPB with excitonic Hopfield coefficient in AFM and FM order, respectively. In the AFM order at 0 T, the LPB redshifts by 2 meV until 33 mW pump power, while it blueshifts with a similar amplitude of 2.3 meV in the FM order at 3 T. Such opposite trends are general for the LPB with same magnetic orders. That is to say, in the case of AFM order, the LPB modes encounter a net redshift for all detuning conditions, while the LPB modes in the FM order experience a contrasting blueshift for all detunings (Supplementary Fig. S4f,g). These trends become also more prominent with increasing excitonic coefficient (Supplementary Fig. S4j), which is an explicit evidence on the magnetic-order and density dependent excitonic interactions mediated by the incoherent magnons<sup>6</sup>.

To gain further insights into the nature of non-linear response, we theoretically investigate the microscopic origin for different non-linear processes that can lead to the observed energy shift (details in Supplementary Note 5). The analysis supports the experimental findings, and qualitatively explains the difference for non-linear response in the case of zero and large magnetic field. As a leading contribution we identified the influence of incoherent magnons that contribute to the

field-dependent optical non-linearity. The corresponding energy shift depends on the magnon mode occupation, and can be parametrized by the effective temperature. The shift is defined as  $\Delta\mathcal{E} \approx \mathcal{A}(B)\rho_X + \mathcal{B}(B)\Delta T$ , where  $\rho_X$  is the exciton density and  $\Delta T$  is the change of magnon temperature. The first term in  $\Delta\mathcal{E}$ , proportional to the  $\mathcal{A}$ -factor, comes from Coulomb-based exciton-exciton (X-X) interactions<sup>34</sup> and non-linear phase space filling effects<sup>35</sup>. Both contributions lead to the blueshift of LBP energy at increasing pump power (exciton occupation  $\rho_X$ ). This blueshift is of non-magnetic origin and is present for both zero and finite magnetic field. Studying the excitons properties in CrSBr, we estimate the corresponding interaction at  $\mathcal{A}(B) = 0.48 \mu\text{eV}\mu\text{m}^2$ , and find that it stays approximately constant in the range from  $B = 0$  to  $B = 3$  T.

The second term in  $\Delta\mathcal{E}$  arises from the coupling between excitonic and magnonic modes, being a signature of the CrSBr material. Here, we need to consider cases of AFM and FM ordering separately. We find that while magnon-based contributions to the non-linearity vanish in zero and saturating magnetic fields, the presence of incoherent magnons however can introduce a strong redshift for the LPB mode in the AFM case. This corresponds to the temperature-dependent term with the  $\mathcal{B}$ -factor, which depends strongly on the underlying magnetic order (see Supplementary Note 5). Analyzing the magnonic spectrum, we find that in AFM case the  $\mathcal{B}$ -factor is significant and can be approximated as  $\mathcal{B}(0) = -32k_B$ , where  $k_B$  is the Boltzmann constant. The overall behaviour corresponds to the redshift, reflecting the experimental observations (Fig. 2). In the FM case, the magnonic contribution is very weak ( $\mathcal{B}(3\text{T}) \approx 0$ ), resulting in a net blueshift. The non-linear shift is predominantly due to the X-X interaction and phase space filling effects, described by the  $\mathcal{A}$ -factor, and corresponding to the repulsive interactions of the polaritons.

The non-linear features of our polaritons become most pronounced in the power-dependent blueshift for pump powers exceeding 33 mW (Figs. 2e,h). The non-linear shift for the LPB in both magnetic orders reaches highest values around 44 mW, before it saturates at even higher pump powers. The maximum blueshift amplitude in FM order is 8.3 meV, significantly larger than the 5.8 meV blueshift in AFM order (Figs. 2e,h). The strong increase of the blueshift in the high density regime can no longer be assigned to X-X interactions but aligns with the saturation of the Rabi-splitting via phase space fill-

ing, which results in a significant blueshift of the  $P_6$  resonance and consequently translates to a similar energy shift of the hybridized open cavity mode. This magnetically controllable non-linear interaction in CrSBr is really unconventional. We note that this saturation behavior, which displays a clear dependency on magnetic order, hints at the interplay between saturation and interlayer localization/delocalization of the exciton wavefunction via spin-allowed layer coupling (Fig. 1b). According to Eq. S(57) of the Supplementary Information, the change from AFM order to FM order leads to a change of around 20 % in the saturation effect.

### Correlations of the exciton-polariton condensates

Polariton condensates are a coherent quantum phase<sup>36</sup>, which displays specific fingerprints in the first-order<sup>25,37</sup> and second-order correlation function<sup>38-41</sup>, especially at the transition from the linear- to the non-linear regime. In the following, we keep the magnetic field geometry and the cavity detuning conditions for the AFM and FM magnetic orders as in Figs. 2a,b, respectively.

First, we probe the emergence of first-order spatio-temporal coherence as a function of the polariton density. The experiment is carried out via a Michelson interferometer with a retro-reflector at the end of the reference arm. The resulting spatially inverted and slightly laterally shifted image is brought to overlap with the delay arm image by a focal lens (See Methods for setup details). A time-delay can be introduced via tuning the delay arm. The emergent interference fringes, which evolve with the polariton density, can be used to deduce the first-order spatio-temporal coherence:

$$g^{(1)}(\vec{r}, \Delta\tau) = \frac{I - I_1 - I_2}{2 \cos(\Delta\phi) \sqrt{I_1 I_2}} \quad (1)$$

where  $I$ ,  $I_1$  and  $I_2$  are the intensities of the interference, delay and reference arms, respectively. The phase difference  $\Delta\phi = \Delta\vec{k} \cdot \vec{r} + \omega \Delta\tau$  is a function of the real-space position  $\vec{r}$  of the interference fringes, wavevector difference  $\Delta\vec{k}$  of the emissions from two arms, frequency  $\omega$  and interferometer time delay  $\Delta\tau$ . We see a clear development of the characteristic spatial interference fringes with the polariton density in both the AFM and FM orders (top panels in Fig. 3a and Supplementary Fig. S8b), which translates to the emergence of first-order correlation that clearly enhances with the excitation power (bottom panels in Fig. 3a and Supplementary Fig. S8b). Details on the data analysis are given in the Methods section.

To have a better notion of the spatial extension of the coherence, we summarize the power dependence of the coherence length  $\lambda_c$  in Fig. 3c. The condensate in AFM order reaches a maximum coherence length  $\lambda_c = 5.1 \mu\text{m}$  at a pump power of  $\sim 30$  mW, while the condensate in FM order reaches its maximum  $\lambda_c = 4.8 \mu\text{m}$  much earlier at  $\sim 25$  mW. This result is consistent with the larger polaritonic non-linearity owing to the expanded exciton wavefunction in the FM order.

A quantum optical characterization of the emergence of coherence in the light-matter coupled system is conducted via measuring the second-order temporal correlation of the condensates. The second-order correlation function reads

$$g^{(2)}(\tau) = \frac{\langle I(t)I(t+\tau) \rangle}{\langle I(t) \rangle \langle I(t+\tau) \rangle} \quad (2)$$

where  $I(t)$  and  $I(t+\tau)$  are the emission intensities that are proportional to the number of photon counts registered at time  $t$  and a delayed time  $t+\tau$ , respectively. The bracket denotes the time average.  $g^{(2)}(\tau)$  characterizes the intensity correlations and thus gives insights into the emission statistics of the system. We are particularly interested in the value at zero delay  $g^{(2)}(0)$ , which distinguishes a classical ( $g^{(2)}(0) > 1$ ) from a coherent ( $g^{(2)}(0) = 1$ ) and sub-Poissonian ( $g^{(2)}(0) < 1$ ) emission statistics<sup>42</sup>.

The experiment is carried out via a Hanbury Brown and Twiss setup<sup>43</sup>, composed of two avalanche photo diodes connected via a timing electronic tagger whose temporal resolution is 350 ps. Therefore, the experiment temporarily averages fully over the emission bursts from the LPB excited by the cavity, which is driven with 200 fs laser pulses with a repetition rate of 76 MHz. Because of the short excitonic lifetime of approximately a few picoseconds in CrSBr<sup>44</sup>, the anticipated  $g^{(2)}(0) = 2$  of the thermal state for the pump power far below the condensate threshold is thus averaged out by the instrumental temporal resolution<sup>45-47</sup>. The main features of this experiment are compiled in Fig. 3b for the AFM order and in Supplementary Fig. S9 for the FM scenario. We notice that the  $g^{(2)}(0)$  in both the AFM and FM phases monotonously decrease from 1.1 towards 1 as the power ramps up. This behavior is independent of the applied magnetic field, and most importantly consolidates the emergence of a macroscopically coherent condensate in our system in both magnetic orders.

## Summary

In conclusion, our work compiles clear fingerprints of the emergence of a coherent condensate of exciton-polaritons in the magnetic van der Waals crystal CrSBr. The condensate is distinct via its power-dependent threshold, its first-order spatio-temporal coherence and second-order temporal coherence. We find a new kind of magnetically tunable non-linearity arising from the strong coupling of excitons with the magnetic order in the material, which pinpoints the importance of the exciton non-linearity and especially the coupling to incoherent magnons for the global behavior of the condensate. Our work is of large interest for experiments seeking to control magnetism with cavity photons, and especially for interfacing coherent condensates with magnetically ordered phases. It enables further studies of new physical phenomena, such as the dynamic coupling of exciton-polariton condensate with the propagating coherent magnons, and polaritonic fluid dressed with skyrmion and vortice textures. Besides the conventional magnetic transport and tunneling structures<sup>48–50</sup>, cavity-mediated devices based on CrSBr can fill a gap in our ever-growing inventory of novel quantum nanophotonic applications such as magnetically controllable and highly non-linear polaritonic Josephson junctions<sup>51,52</sup>.

## Reference

1. Gibertini, M., Koperski, M., Morpurgo, A. F. & Novoselov, K. S. Magnetic 2d materials and heterostructures. *Nature Nanotechnology* **14**, 408–419 (2019).
2. Ye, C. *et al.* Layer-dependent interlayer antiferromagnetic spin reorientation in air-stable semiconductor crsbr. *ACS Nano* **16**, 11876–11883 (2022).
3. Wilson, N. P. *et al.* Interlayer electronic coupling on demand in a 2d magnetic semiconductor. *Nature Materials* **20**, 1657–1662 (2021).
4. Tabataba-Vakili, F. *et al.* Doping-control of excitons and magnetism in few-layer crsbr. *Nature Communications* **15**, 4735 (2024).
5. Lin, K. *et al.* Strong exciton–phonon coupling as a fingerprint of magnetic ordering in van der waals layered crsbr. *ACS Nano* **18**, 2898–2905 (2024).
6. Dimberger, F. *et al.* Magneto-optics in a van der waals magnet tuned by self-hybridized polaritons. *Nature* **620**, 533–537 (2023).
7. Komar, R. *et al.* Colossal magneto-excitonic effects in 2d van der waals magnetic semiconductor crsbr. *arXiv preprint arXiv:2409.00187* (2024).
8. Linhart, W. *et al.* Optical markers of magnetic phase transition in crsbr. *Journal of Materials Chemistry C* **11**, 8423–8430 (2023).
9. Lee, K. *et al.* Magnetic order and symmetry in the 2d semiconductor crsbr. *Nano Letters* **21**, 3511–3517 (2021).
10. Rizzo, D. J. *et al.* Visualizing atomically layered magnetism in crsbr. *Advanced Materials* **34**, 2201000 (2022).
11. Heißenbüttel, M.-C. *et al.* Quadratic optical response of crsbr controlled by spin-selective inter-layer coupling. *arXiv preprint arXiv:2403.20174* (2024).
12. Cenker, J. *et al.* Reversible strain-induced magnetic phase transition in a van der waals magnet. *Nature Nanotechnology* **17**, 256–261 (2022).
13. Pawbake, A. *et al.* Magneto-optical sensing of the pressure driven magnetic ground states in bulk crsbr. *Nano Letters* **23**, 9587–9593 (2023).
14. Datta, B. *et al.* Magnon-mediated exciton-exciton interaction in a van der waals antiferromagnet. *arXiv preprint arXiv:2409.18501* (2024).
15. Bae, Y. J. *et al.* Exciton-coupled coherent magnons in a 2d semiconductor. *Nature* **609**, 282–286 (2022).
16. Diederich, G. M. *et al.* Tunable interaction between excitons and hybridized magnons in a layered semiconductor. *Nature Nanotechnology* **18**, 23–28 (2023).
17. Wang, T. *et al.* Magnetically-dressed crsbr exciton-polaritons in ultrastrong coupling regime. *Nature Communications* **14**, 5966 (2023).
18. Li, Q. *et al.* Two-dimensional magnetic exciton polariton with strongly coupled atomic and photonic anisotropies. *Physical Review Letters* **133**, 266901 (2024).
19. Ruta, F. L. *et al.* Hyperbolic exciton polaritons in a van der waals magnet. *Nature Communications* **14**, 8261 (2023).
20. Hopfield, J. Theory of the contribution of excitons to the complex dielectric constant of crystals. *Physical Review* **112**, 1555 (1958).

21. Dusel, M. *et al.* Room temperature organic exciton-polariton condensate in a lattice. *Nature Communications* **11**, 2863 (2020).
22. Horneber, D. *et al.* Enwrapped perylene bisimide enables room temperature polariton lasing and photonic lattices. *arXiv preprint arXiv:2409.12093* (2024).
23. Dufferwiel, S. *et al.* Strong exciton-photon coupling in open semiconductor microcavities. *Applied Physics Letters* **104** (2014).
24. Weisbuch, C., Nishioka, M., Ishikawa, A. & Arakawa, Y. Observation of the coupled exciton-photon mode splitting in a semiconductor quantum microcavity. *Physical Review Letters* **69**, 3314 (1992).
25. Kasprzak, J. *et al.* Bose-einstein condensation of exciton polaritons. *Nature* **443**, 409–414 (2006).
26. Tempel, J.-S. *et al.* Characterization of two-threshold behavior of the emission from a gaas microcavity. *Physical Review B—Condensed Matter and Materials Physics* **85**, 075318 (2012).
27. Bajoni, D. *et al.* Polariton laser using single micropillar gaas-gaalas semiconductor cavities. *Physical Review Letters* **100**, 047401 (2008).
28. Tempel, J.-S. *et al.* Temperature dependence of pulsed polariton lasing in a gaas microcavity. *New Journal of Physics* **14**, 083014 (2012).
29. Chernikov, A., Ruppert, C., Hill, H. M., Rigosi, A. F. & Heinz, T. F. Population inversion and giant bandgap renormalization in atomically thin w<sub>s</sub>2 layers. *Nature Photonics* **9**, 466–470 (2015).
30. Wang, G. *et al.* Colloquium: Excitons in atomically thin transition metal dichalcogenides. *Reviews of Modern Physics* **90**, 021001 (2018).
31. Klein, J. *et al.* The bulk van der waals layered magnet crsbr is a quasi-1d material. *ACS Nano* **17**, 5316–5328 (2023).
32. Smolenski, S. *et al.* Large exciton binding energy in the bulk van der waals magnet crsbr. *arXiv preprint arXiv:2403.13897* (2024).
33. Semina, M. *et al.* Excitons and trions in crsbr bilayers. *arXiv preprint arXiv:2411.15493* (2024).
34. Shahnazaryan, V., Iorsh, I., Shelykh, I. A. & Kyriienko, O. Exciton-exciton interaction in transition-metal dichalcogenide monolayers. *Physical Review B* **96**, 115409 (2017).
35. Song, K. W., Chiavazzo, S. & Kyriienko, O. Microscopic theory of nonlinear phase space filling in polaritonic lattices. *Physical Review Research* **6**, 023033 (2024).
36. Snoke, D. Spontaneous bose coherence of excitons and polaritons. *Science* **298**, 1368–1372 (2002).
37. Deng, H., Solomon, G. S., Hey, R., Ploog, K. H. & Yamamoto, Y. Spatial coherence of a polariton condensate. *Physical Review Letters* **99**, 126403 (2007).
38. Deng, H., Weihs, G., Santori, C., Bloch, J. & Yamamoto, Y. Condensation of semiconductor microcavity exciton polaritons. *Science* **298**, 199–202 (2002).
39. Kasprzak, J. *et al.* Second-order time correlations within a polariton bose-einstein condensate in a cdte microcavity. *Physical Review Letters* **100**, 067402 (2008).
40. Love, A. *et al.* Intrinsic decoherence mechanisms in the microcavity polariton condensate. *Physical Review Letters* **101**, 067404 (2008).
41. Fischer, J. *et al.* Spatial coherence properties of one dimensional exciton-polariton condensates. *Physical Review Letters* **113**, 203902 (2014).
42. Loudon, R. *The quantum theory of light* (OUP Oxford, 2000).
43. Brown, R. H. & Twiss, R. Q. Correlation between photons in two coherent beams of light. *Nature* **177**, 27–29 (1956).
44. Meineke, C. *et al.* Ultrafast exciton dynamics in the atomically thin van der waals magnet crsbr. *Nano Letters* **24**, 4101–4107 (2024).
45. Shan, H. *et al.* Second-order temporal coherence of polariton lasers based on an atomically thin crystal in a microcavity. *Physical Review Letters* **131**, 206901 (2023).
46. Klaas, M. *et al.* Evolution of temporal coherence in confined exciton-polariton condensates. *Physical Review Letters* **120**, 017401 (2018).
47. Wiersig, J. *et al.* Direct observation of correlations between individual photon emission events of a microcavity laser. *Nature* **460**, 245–249 (2009).

48. Chen, Y. *et al.* Twist-assisted all-antiferromagnetic tunnel junction in the atomic limit. *Nature* 1–7 (2024).
49. Boix-Constant, C. *et al.* Multistep magnetization switching in orthogonally twisted ferromagnetic monolayers. *Nature Materials* **23**, 212–218 (2024).
50. Telford, E. J. *et al.* Layered antiferromagnetism induces large negative magnetoresistance in the van der waals semiconductor crsbr. *Advanced Materials* **32**, 2003240 (2020).
51. Abbarchi, M. *et al.* Macroscopic quantum self-trapping and josephson oscillations of exciton polaritons. *Nature Physics* **9**, 275–279 (2013).
52. Lagoudakis, K. G., Pietka, B., Wouters, M., André, R. & Deveaud-Plédran, B. Coherent oscillations in an exciton-polariton josephson junction. *Physical Review Letters* **105**, 120403 (2010).
53. Savona, V., Andreani, L., Schwendimann, P. & Quattropani, A. Quantum well excitons in semiconductor microcavities: Unified treatment of weak and strong coupling regimes. *Solid State Communications* **93**, 733–739 (1995).
54. Castellanos-Gomez, A. *et al.* Deterministic transfer of two-dimensional materials by all-dry viscoelastic stamping. *2D Materials* **1**, 011002 (2014).
55. Tschudin, M. A. *et al.* Imaging nanomagnetism and magnetic phase transitions in atomically thin crsbr. *Nature Communications* **15**, 6005 (2024).
56. Kappei, L., Szczytko, J., Morier-Genoud, F. & Deveaud, B. Direct observation of the mott transition in an optically excited semiconductor quantum well. *Physical review letters* **94**, 147403 (2005).
57. Huber, R., Kaindl, R. A., Schmid, B. A. & Chemla, D. S. Broadband terahertz study of excitonic resonances in the high-density regime in  $\text{GaAs}/\text{Al}_x\text{Ga}_{1-x}$  as quantum wells. *Physical Review B—Condensed Matter and Materials Physics* **72**, 161314 (2005).
58. Rossbach, G. *et al.* High-temperature mott transition in wide-band-gap semiconductor quantum wells. *Physical Review B* **90**, 201308 (2014).
59. Cain, N. *et al.* Photoluminescence of  $\text{CdTe}/\text{CdMnTe}$  multiple quantum wells excited near the mott transition. *Journal of luminescence* **75**, 269–275 (1997).
60. Teran, F., Chen, Y., Potemski, M., Wojtowicz, T. & Karczewski, G. Optical properties of  $\text{Cd}_{1-x}\text{Mn}_x\text{Te}$  quantum wells across the mott transition: An interband spectroscopy study. *Physical Review B—Condensed Matter and Materials Physics* **73**, 115336 (2006).
61. Ziebel, M. E. *et al.* Crsbr: an air-stable, two-dimensional magnetic semiconductor. *Nano Letters* **24**, 4319–4329 (2024).
62. Wu, F. *et al.* Quasi-1d electronic transport in a 2d magnetic semiconductor. *Advanced Materials* **34**, 2109759 (2022).
63. Liu, W. *et al.* A three-stage magnetic phase transition revealed in ultrahigh-quality van der waals bulk magnet crsbr. *ACS nano* **16**, 15917–15926 (2022).
64. Scholes, G. D. Insights into excitons confined to nanoscale systems: electron–hole interaction, binding energy, and photodissociation. *ACS nano* **2**, 523–537 (2008).
65. Nguyen, D.-T. *et al.* Excitonic nonlinearities in single-wall carbon nanotubes. *physica status solidi (b)* **249**, 907–913 (2012).
66. Nguyen, D. *et al.* Excitonic homogeneous broadening in single-wall carbon nanotubes. *Chemical Physics* **413**, 102–111 (2013).
67. Wang, F., Dukovic, G., Brus, L. E. & Heinz, T. F. The optical resonances in carbon nanotubes arise from excitons. *Science* **308**, 838–841 (2005).
68. Lauret, J. *et al.* Optical transitions in single-wall boron nitride nanotubes. *Physical review letters* **94**, 037405 (2005).
69. Wirtz, L., Marini, A. & Rubio, A. Excitons in boron nitride nanotubes: dimensionality effects. *Physical review letters* **96**, 126104 (2006).
70. Cassabois, G., Valvin, P. & Gil, B. Hexagonal boron nitride is an indirect bandgap semiconductor. *Nature photonics* **10**, 262–266 (2016).
71. Kavokin, A., Baumberg, J. J., Malpuech, G. & Laussy, F. P. *Microcavities* (Oxford university press, 2017).
72. Klingshirn, C. F. *Semiconductor Optics* (Springer Science & Business Media, 2012).



73. Mott, N. F. The basis of the electron theory of metals, with special reference to the transition metals. *Proceedings of the Physical Society. Section A* **62**, 416 (1949).
74. Mott, N. *Metal-insulator transitions* (CRC Press, 2004).
75. Ceferino, A., Song, K. W., Magorrian, S. J., Zólyomi, V. & Fal'ko, V. I. Crossover from weakly indirect to direct excitons in atomically thin films of inse. *Physical Review B* **101**, 245432 (2020).
76. Danovich, M. *et al.* Localized interlayer complexes in heterobilayer transition metal dichalcogenides. *Physical Review B* **97**, 195452 (2018).
77. López-Paz, S. A. *et al.* Dynamic magnetic crossover at the origin of the hidden-order in van der waals antiferromagnet crsbr. *Nature Communications* **13** (2022).
78. Keldysh, L. V. Coulomb interaction in thin semiconductor and semimetal films. *Soviet Journal of Experimental and Theoretical Physics Letters* **29**, 658 (1979).
79. Rytova, N. The screened potential of a point charge in a thin film. *Moscow University Physics Bulletin* **3**, 18 (1967).
80. Cudazzo, P., Tokatly, I. V. & Rubio, A. Dielectric screening in two-dimensional insulators: Implications for excitonic and impurity states in graphane. *Physical Review B* **84**, 085406 (2011).
81. Song, K. W. & Kyriienko, O. Electrically tunable and enhanced nonlinearity of moiré exciton-polaritons in transition metal dichalcogenide bilayers. *arXiv e-prints arXiv:2406.08263* (2024).
82. Wang, Y., Luo, N., Zeng, J., Tang, L.-M. & Chen, K.-Q. Magnetic anisotropy and electric field induced magnetic phase transition in the van der waals antiferromagnet crsbr. *Physical Review B* **108**, 054401 (2023).

## Methods

**CrSBr crystal synthesis** CrSBr crystals were synthesized through the direct reaction from the elements using chemical vapor transport method. High-purity chromium (99.99 %, -60 mesh, Chemsavers, USA),

bromine (99.9999 %, Sigma-Aldrich, Czech Republic), and sulfur (granules, 99.9999 %, Stanford Materials, USA) were combined in stoichiometric ratio within a quartz ampoule (35×220 mm) corresponding to 15 g of CrSBr. An excess of 0.5 g bromine was employed to enhance vapor transport. The material was pre-reacted within an ampoule utilizing a crucible furnace gradually heated on 400°C, 500°C, 600°C and 700 °C for 24 hours at each step, while the second end of the ampoule was kept below 250 °C. Subsequently, the ampoule was positioned within a horizontal two-zone furnace to facilitate crystal growth. Initially, the temperature of growth zone was heated to 900 °C, while the source zone was heated to 700 °C for 25 hours. For the growth, the thermal gradient was reversed and the source zone was heated on 900 °C and the growth zone on 800°C over a period of 10 days. The crystals with dimensions of up to 3×10 mm<sup>2</sup> were removed from the ampoule in an Ar glovebox.

**Transfer matrix simulation** We consider the normal incidence with a unity field intensity. The transfer matrix  $T(l)$  across a dielectric layer of thickness  $l$  is

$$T(l) = \begin{bmatrix} \cos kl & \frac{i}{\tilde{n}} \sin kl \\ i\tilde{n} \sin kl & \cos kl \end{bmatrix}, \quad (3)$$

where  $k=2\pi\tilde{n}/\lambda$  is the wavevector and  $\tilde{n}(\lambda)=n+i\kappa$  is the wavelength dependent complex refractive index of the homogeneous layer material. The real and imaginary parts of the refractive index of CrSBr are presented in Supplementary Fig. S1e. The total transfer matrix over a structure containing  $m$  layers is  $T_{\text{tot}}=\prod_{i=1}^m T_i$ , where  $T_i$  is the transfer matrix of the  $i$ th layer in the structure. The reflectivity and transmission of the whole structure are

$$R = \left| \frac{\tilde{n}_{\text{sub}}(T_{11} + T_{12}) - (T_{21} + T_{22})}{\tilde{n}_{\text{sub}}(-T_{11} + T_{12}) + (T_{21} - T_{22})} \right|^2, \quad (4)$$

$$T = \tilde{n}_{\text{sub}} \left| \frac{2(T_{12}T_{21} - T_{11}T_{22})}{\tilde{n}_{\text{sub}}(-T_{11} + T_{12}) + (T_{21} - T_{22})} \right|^2, \quad (5)$$

where  $\tilde{n}_{\text{sub}}$  is the refractive index of the semi-infinite substrate material (SiO<sub>2</sub>) underneath the bottom DBR, and  $T_{jk}$  is the element on the  $j$ th row and  $k$ th column of the transfer matrix  $T_{\text{tot}}$ . The absorption can be obtained via  $A=I-R-T$ .

### Coupled oscillator model

$$\begin{bmatrix} E_{c_1} & 0 & 0 & \frac{V_1}{2} & \frac{V_2}{2} & \frac{V_3}{2} & \frac{V_4}{2} & \frac{V_5}{2} & \frac{V_6}{2} \\ 0 & E_{c_2} & 0 & \frac{V_1}{2} & \frac{V_2}{2} & \frac{V_3}{2} & \frac{V_4}{2} & \frac{V_5}{2} & \frac{V_6}{2} \\ 0 & 0 & E_{c_3} & \frac{V_1}{2} & \frac{V_2}{2} & \frac{V_3}{2} & \frac{V_4}{2} & \frac{V_5}{2} & \frac{V_6}{2} \\ \frac{V_1}{2} & \frac{V_1}{2} & \frac{V_1}{2} & E_{P_1} & 0 & 0 & 0 & 0 & 0 \\ \frac{V_2}{2} & \frac{V_2}{2} & \frac{V_2}{2} & 0 & E_{P_2} & 0 & 0 & 0 & 0 \\ \frac{V_3}{2} & \frac{V_3}{2} & \frac{V_3}{2} & 0 & 0 & E_{P_3} & 0 & 0 & 0 \\ \frac{V_4}{2} & \frac{V_4}{2} & \frac{V_4}{2} & 0 & 0 & 0 & E_{P_4} & 0 & 0 \\ \frac{V_5}{2} & \frac{V_5}{2} & \frac{V_5}{2} & 0 & 0 & 0 & 0 & E_{P_5} & 0 \\ \frac{V_6}{2} & \frac{V_6}{2} & \frac{V_6}{2} & 0 & 0 & 0 & 0 & 0 & E_{P_6} \end{bmatrix} \quad (6)$$

In this extended coupled oscillator model<sup>53</sup>, the coupling matrix  $M$ .(6) includes six self-hybridized polaritons and the ground transverse cavity modes from three longitudinal mode orders. The additional two transverse modes ( $E_{c_1}$  and  $E_{c_3}$ ) are taken into account for the unconventional crossing through the self-hybridized  $P_6$  polaritons at very small or very large detunings (Fig. 1d and Supplementary Fig. S4a,b). The off-diagonal terms represent the half coupling strengths between the transverse modes and self-hybridized polaritons. The energy of the transverse cavity modes is a function of the applied DC Voltages. Diagonalizing this matrix allows us to extract the dispersions of the new exciton-polariton modes as a function of the DC Voltage for the CrSBr flake in our tunable microcavity. Other higher energy polariton modes can also be fitted separately with this coupling matrix by considering transverse modes with same symmetry.

**Cryogenic open cavity preparation** The indentation into the mesa surface are 300 nm deep for all of the concave structures whose diameters vary from 3  $\mu\text{m}$  to 6  $\mu\text{m}$ . These indentations were etched by  $\text{Ga}^+$  focused ion beam lithography (FEI Helios 600i). DBR mirrors were then sputtered on top of the mesa and silica wafer, respectively. The DBR on the mesa contains 8 pairs of 157 nm  $\text{SiO}_2$  and 99 nm  $\text{TiO}_2$ , yielding a stop band center at 1.3745 eV (902 nm). The bottom DBR mirror contains 8 pairs of 181 nm  $\text{SiO}_2$  and 111 nm  $\text{TiO}_2$ , yielding a stop band center at 1.2155 eV (1020 nm). The CrSBr flake was exfoliated and transferred on the bottom DBR mirror by a dry-stamping method<sup>54</sup>. The thickness of the flake was measured in an atomic force microscope (WITec: alpha300 RA) in tapping mode. The entire open optical microcavity was submerged in a heat-exchange helium gas that has a pressure of 20 mbar at room temperature. The microscope images of mesa and CrSBr flake are compiled in Supplementary Fig. S1. The open cavity was then loaded into a closed-cycle cryostat (attocube: attoDRY1000). All of the experiments were

performed at a sample temperature of 3.5 K. The piezo-based nano-positioners have a sub-nanometer detuning increment and are ultra-stable to maintain a certain cavity length.

**Optical microscopy** The optical setup is in a confocal geometry. For the PL measurements in Fig. 1, we used a 725 nm laser excitation with a 5 ps pulse duration and 78 MHz repetition rate, which was generated from a super-continuum white light laser and an acousto-optic tunable filter (NKT Photonics: SuperK SELECT). For the pump-power dependent PL measurements in Fig. 2, the 725 nm laser excitation of 200 fs pulse width and 76 MHz repetition rate is generated from a mode-locked Ti-sapphire laser (Coherent: Mira 900 Femtosecond). Laser excitation and signal collection were realized by a long work-distance lens objective (Thorlabs: 354105-B, NA=0.6, f=5.5 mm) that focused on the surface of the top DBR. The static PL signals were transmitted in free-space, collected and focused by a plano-convex lens (f=450 mm) on the spectrometer slit (Andor: Shamrock SR-500i). The signals were then dispersed by a 600  $\text{mm}^{-1}$  grating and recorded by a charge coupled device (CCD, Andor: iKon-M 934).

**First order correlation measurements** First-order correlation was measured via a Michelson interferometer. We firstly used the spectrometer to disperse the static PL signal and filtered the spectral window of the LPB by using edge filters (Semrock: TLP01-995 and TSP01-995). The interferometer then divided the filtered signal into the reference and delay arms. The delay arm has a silver mirror on a kinematic mount, while the reference arm has a retroreflector (Thorlabs: PS976M) that reflects back a spatially displaced and inverted image. The reflections of two arms were collected by the same plano-convex lens (f=450 mm) to focus the signals on the spectrometer slit. The grating was then set to zero-order to check the real-space emissions from the reference and delay arms. We adjusted the angle of the delay arm mirror to spatially overlap the signals on the CCD. The zero-delay position was affirmed by the maximum interference fringe visibility. We then recorded the excitation power dependence at zero delay of the delay arm, reference arm and interference images.  $g^{(1)}(\vec{r}, \Delta\tau)2 \cos(\Delta\phi)$  can be readily obtained from the captured interference, delay and reference arms images via Eq. 1. To remove the phase factor, we applied the two-dimensional fast Fourier transform (FFT) on the real space  $g^{(1)}(\vec{r}, \Delta\tau)2 \cos(\Delta\phi)$  (using WaveMetrics Igor Pro), yielding two Fourier peaks in the momentum-space. One Fourier peak was then

filtered and displaced to the center ( $k_x=0$ ,  $k_y=0$ ) of the momentum-space. A following inverse fast Fourier transform (IFFT) brought the complex  $g^{(1)}(\vec{r}, \Delta\tau)$  back to the real-space. The amplitude of the spatially dependent  $g^{(1)}(\vec{r}, 0)$  was then calculated for the condensate in AFM and FM orders, and showed in Fig. 3a and Supplementary Fig. S8b, respectively.

**Second order Correlation measurements** The second order correlation was measured in a Hanbury Brown and Twist interferometry. The filtered signal was then collected by a fiber-coupled zoom collimator (Thorlabs: ZC618APC-B), whose output coupled with one input channel of a  $2\times 2$  fiber beam splitter (Thorlabs: TW850R5A2), while the second input was idle. The outputs of the fiber beam splitter connected to two same APDs (Laser components: Count T) whose electronic output was sent to the time correlator (Swabian instruments: Time-Tagger 20). A 250 ps binning width was used for these time-correlated measurements to match the APD temporal resolution (350 ps).

#### Data availability

All data are in the main text or the Supplementary materials.

**Acknowledgments** C.S., B.H. and L.L. gratefully acknowledge funding from the Deutsche Forschungsgemeinschaft

(DFG) in the framework of SPP 2244 (funding number: Schn1376/14-2). V.S. acknowledges DFG (funding number: INST 184/222-1). B.H. acknowledges the Alexander von Humboldt-Stiftung for the fellowship grant. M.E. acknowledges funding from the University of Oldenburg through a Carl von Ossietzky Young Researchers' Fellowship. F.E. acknowledges support by DFG SFB 1375 (NOA) and BMBF FKZs 1CKISQ087K and 13XP5053A. K.W.S. and O.K. acknowledge the support from UK EPSRC grant EP/X017222/1. Z.S. and J.R. were supported by ERC-CZ program (project LL2101) from Ministry of Education Youth and Sports (MEYS) and by the project Advanced Functional Nanorobots (reg. No. CZ.02.1.01/0.0/0.0/15\_003/0000444 financed by the ERDF).

**Author contributions** C.S. conceived of the experiments. Z.S. and J.R. synthesized the CrSBr crystals. F.E. and M.E. prepared and manufactured the mesa and DBR mirrors. B.H. and H.S. assembled the sample and cavity. V.S. and B.H. measured the atomic force microscopy. B.H., H.S. and L.L. performed the measurements. C.S. supervised the experiments. B.H. analyzed the experimental data with assistance from H.S. K.W.S. and O.K. provided theoretical interpretations. All authors discussed the results. B.H., C.S., K.W.S. and O.K. wrote the manuscript with inputs from all authors.

**Competing interests** The authors declare no competing interests.

#### Supplementary information

**Correspondence and requests for materials** should be addressed to Christian Schneider.

## Supplementary information: Exciton-polariton condensate in the van der Waals magnet CrSBr

Bo Han<sup>1,7</sup>, Hangyong Shan<sup>1,7</sup>, Kok Wee Song<sup>2</sup>, Lukas Lackner<sup>1</sup>, Martin Esmann<sup>1</sup>, Vita Solovyeva<sup>1</sup>, Falk Eilenberger<sup>3,4,5</sup>, Jakub Regner<sup>6</sup>, Zdeněk Sofer<sup>6</sup>, Oleksandr Kyriienko<sup>2</sup> and Christian Schneider<sup>1,\*</sup>

<sup>1</sup>*Institute of Physics, Faculty V, Carl von Ossietzky University Oldenburg, 26129 Oldenburg, Germany.*

<sup>2</sup>*Department of Physics and Astronomy, University of Exeter, Exeter EX4 4QL, United Kingdom.*

<sup>3</sup>*Institute of Applied Physics, Abbe Center of Photonics, Friedrich Schiller Universität Jena, 07745 Jena, Germany.*

<sup>4</sup>*Fraunhofer-Institute for Applied Optics and Precision Engineering IOF, 07745 Jena, Germany.*

<sup>5</sup>*Max Planck School of Photonics, 07745 Jena, Germany.*

<sup>6</sup>*Department of Inorganic Chemistry, Faculty of Chemical Technology, University of Chemistry and Technology Prague, Technická 5, Prague 6, 16628, Czech Republic.*

<sup>7</sup>*These authors contributed equally.*

\* *E-mail: christian.schneider@uni-oldenburg.de*

### Contents

- Supplementary note 1: Further details of sample and cavity structures
- Supplementary note 2: Optical properties of sample position 2
- Supplementary note 3: Polariton non-linearity measurements
- Supplementary note 4: Exciton density estimation
- Supplementary note 5: Theoretical model for exciton-magnon coupling
- Supplementary note 6: Correlation measurements of the polariton condensates in FM order
- Supplementary Table. S1: Self-hybridized polariton energies and coupling strengths
- Supplementary Fig. S1: Cavity and material properties
- Supplementary Fig. S2: Magneto-PL of sample position 1 at different cavity detunings
- Supplementary Fig. S3: Pump power dependent PL measurements of sample position 2
- Supplementary Fig. S4: LPB non-linearity with different cavity detunings and magnetic orders
- Supplementary Fig. S5: Simulation of full cavity structure
- Supplementary Fig. S6: Schematic diagram for the spin model in bilayer CrSBr
- Supplementary Fig. S7: Power dependent PL of cavity detuning on sample position 2 (AFM, 0 T)
- Supplementary Fig. S8: First-order correlation of the exciton-polariton condensate at 3 T
- Supplementary Fig. S9: Second-order correlation of the exciton-polariton condensate

## Supplementary note 1: Further details of sample and cavity structures

**Polarization-resolved measurements.** The polarizers on the excitation and detection are aligned to the crystallographic b-axis by searching for the maximum PL emission intensity. A half waveplate on the detection side rotates the polarization of the signal to realize the polarization-resolved measurements. Supplementary Fig. 1f shows that the PL emission of a LPB mode of CrSBr in the external cavity is linearly polarized along the crystal b-axis. The fit yields a unity polarization degree along the crystallographic b-axis.

**Cavity Q-factor.** Figure. S1e contains the reflection of an empty cavity with a gap of 4025 nm, which is simulated by the transfer matrix method. For this geometry, two sharp cavity modes present in the energy range of the self-hybridized polaritons. The mode at 1.353 eV has a Q-factor of 5700, while the other mode at 1.249 eV has a Q-factor of 8600. Although the simulated quality factor (Q-factor) by the transfer matrix methods for our symmetrical dielectric cavity structure is above 5000, the measured Q-factor $\sim$ 1100 of the transverse modes is substantially smaller than the simulated result. The discrepancy is caused by the vibration of the cavity length, which is in a same frequency  $\sim$ 1.4 Hz as the closed-cycle helium pulses. As a result, the cavity resonance is broadened up to  $\sim$ 1.1 meV (see Figs. 2d,g of the manuscript). We note that the considerably compromised Q-factor is still much larger than the Q-factors of cavity structures in previous works (Q-factor $\sim$ 300) using the hybrid of metallic and dielectric mirrors<sup>6,17</sup>. It also does not impede us from the strong light-matter coupling regime and the exciton-polariton condensate.

## Supplementary note 2: Optical properties of sample position 1 and 2

Figure 1d of the manuscript presents the cavity detuning PL on sample position 1. Fig. S4a-c present the cavity detuning PL on sample position 2 in different magnetic orders. The measurements on position 2 are performed with 0.5 mW pulsed laser (725 nm, 200 fs pulse width and 76 MHz repetition rate) at cryogenic temperature of 3.5 K. At 0 T, sample position 2 also exhibits six self-hybridized polariton states ( $P_1$ - $P_6$ ) as position 1. The energies of the self-hybridized polaritons used in the fitting and the coupling strengths are all summarized in Table. S1. We note that the experimentally extracted coupling strengths of the self-hybridized polaritons are nearly constant in both magnetic orders.

	$P_1$	$P_2$	$P_3$	$P_4$	$P_5$	$P_6$	$V_1$	$V_2$	$V_3$	$V_4$	$V_5$	$V_6$
Pos. 1 (AFM)	1.3604	1.3578	1.3540	1.3480	1.3341	1.2895	3.0	4.6	5.6	8.0	15.4	33.0
Pos. 2 (AFM)	1.3660	1.3634	1.3597	1.3540	1.3395	1.2944	4.0	5.0	5.6	9.0	16.4	37.4
Pos. 2 (FM)	1.3515	1.3482	1.3442	1.3376	1.3248	1.2827	4.6	4.6	5.2	9.0	16.4	36.0

**Supplementary Table. S1| Self-hybridized polariton energies and coupling strengths.** The polaritonic energies ( $P_1$ - $P_6$ ) are in unit of eV, while the coupling strengths ( $V_1$ - $V_6$ ) are in unit of meV.

## Supplementary note 3: Polariton non-linearity measurements

Polaritonic non-linearities with different cavity detunings and magnetic orders are obtained via PL measurements on sample position 2. For each power dependent study, we keep the cavity detuning (voltage) constant between 32-52 V as in Fig. S4a for the AFM order (0 T) and 22-46 V as in Fig. S4b for the FM order (3 T). The experimental results are compiled in Fig. S3. The energy shifts of the lowest LPBs are then fitted and summarized in Figs. S4d,e.

For all detuning cases in the AFM order, the LPB firstly experience a moderate linear redshift, and then a giant blueshift follows until the condensate depletes. However, for the detuning cases in the FM order, the energy slope of LPB at low pump powers changes sign from moderate redshift to moderate blueshift, as the detuning voltage is tuned above 36 V in Fig. S4b. And at high pump powers, the giant blueshift in FM order is similar to that in AFM order. By using a linear fit of the LPB energy shifts below 20 mW, the energy slopes (empty spherical symbols) for different

detuning scenarios and magnetic orders are obtained and summarized in Fig. S4j.

We can see that the energy shifts in low power range of the LPB in AFM and FM orders present obviously opposite trends. As the LPB becomes more excitonic (at higher DC voltages), the redshift slope of the LPB in the AFM order becomes smaller (larger amplitude), while in the FM order the slope keeps increasing. This magnetic order dependent phenomena have been observed for the magnetic excitons in CrSBr as a result of coupling to the incoherent magnons that are excited by the temperature<sup>6</sup>. In addition, we note that the redshift should not exist for the highly photonic LPB (22 V) in the FM order because of the much reduced excitonic components and correspondingly little interaction between excitons and incoherent magnons. This effect is actually caused by the redshift of the cavity modes due to the thermal expansion of our open cavity as pump power ramps up. Another proof of cavity thermal expansion is that the extrapolation of the slope value in the AFM order towards the pure photonic regime converges with the FM scenario around -0.05 meV/mW, which is supposed to be the pure contribution from the cavity thermal drift.

To quantify the redshift due to the cavity drift, we need to know the photonic Hopfield coefficients that are specifically contributed by the external cavity modes. Figs. S4h,i show the Hopfield coefficients of the LPB mode in AFM and FM orders, respectively, which are calculated by using a  $2 \times 2$  coupled oscillator model that considers only the  $P_6$  self-hybridized polariton mode and the  $C_2$  cavity mode:

$$\begin{pmatrix} E_{c_2} & V_6/2 \\ V_6/2 & E_{P_6} \end{pmatrix} \quad (7)$$

$$E_{\text{LPB}} = \frac{1}{2} [E_{c_2} + E_{P_6} - \sqrt{V_6^2 + (E_{c_2} - E_{P_6})^2}] \quad (8)$$

$$|P_6|^2 = \frac{1}{2} + \frac{E_{c_2} - E_{P_6}}{2\sqrt{(E_{c_2} - E_{P_6})^2 + V_6^2}} \quad (9)$$

$$|C_2|^2 = \frac{1}{2} - \frac{E_{c_2} - E_{P_6}}{2\sqrt{(E_{c_2} - E_{P_6})^2 + V_6^2}} \quad (10)$$

This model is valid for two reasons. Firstly, the energy difference between  $P_5$  and  $P_6$  intrinsic polaritonic modes is larger than the coupling strength  $V_6$ , so that the strong coupling of  $P_6$  to the external cavity modes can be regarded as independent of other self-hybridized polariton resonances ( $P_1$ - $P_5$ ). Secondly, the usage of two additional cavity modes in our  $9 \times 9$  coupled oscillator model in Figs. S4a,b only becomes vital for unconventional polariton dispersion in either highly photonic ( $\sim 5$  V) or highly excitonic ( $\sim 60$  V) cases, so that utilizing only the middle cavity mode ' $c_2$ ' has negligible influence to the detunings where the polaritonic non-linearities (Fig. S3) are measured.

We note that the Hopfield coefficients in Figs. S4h,i only represent the proportionalities of  $P_6$  self-hybridized polariton and the external cavity mode in the LPB. The excitonic and total photonic Hopfield coefficients should be renormalized by taking into account the intrinsic self-hybridization in our CrSBr flake. For example, using the methods provided in a previous work<sup>6</sup>, the excitonic Hopfield coefficient of  $P_6$  mode with a total magnetic shift of -13.3 meV (left panel of Fig. 1e in the manuscript), is determined as  $|X|_{P_6}^2 = 0.76$ . In presence of an external cavity, the excitonic admixture will be further diluted. For the lowest LPBs in Fig. S4c (44 V, 0 T and 38 V, 3 T on position 2), the Hopfield coefficient of  $P_6$  self-hybridized polariton is  $|P_6|^2 = 0.74$ , which means the LPB has an excitonic Hopfield coefficient  $|X|^2 = |X|_{P_6}^2 \times |P_6|^2 = 0.56$  and total photonic Hopfield coefficient  $|C|^2 = 0.44$ . These results are consistent with the  $|X|^2 = 0.49$  and  $|C|^2 = 0.51$  of the lowest LPB in a similar cavity detuning scenario (36 V) on sample position 1 (see Fig. S2), which is directly calculated by using its magnetic shift.

In the following, we calibrate the polariton non-linearity by removing the contribution from cavity redshifts with increasing pump power. We use the experimentally extracted redshift slope  $s = -0.0474$  meV/mW of the LPB mode at 22 V cavity detuning ( $|C_2|^2 = 0.907$ ) of the FM order to calculate the pure cavity drift slope due to the thermal expansion:  $s_0 = \frac{s}{|C_2|^2} = -0.0523$  meV/mW. We then use  $s_0$  to renormalize the cavity redshift slope of each detuning by

multiplying their photonic Hopfield coefficients  $|C_2|^2$ . We obtain the redshift caused by the cavity thermal expansion  $\delta = s_0 P$ , where  $P$  is the pump power. The LPB mode energy modified by the cavity drift is

$$E'_{\text{LPB}} = \frac{1}{2}[E_{c_2} + E_{P_6} + \delta - \sqrt{V_6^2 + (E_{c_2} + \delta - E_{P_6})^2}]. \quad (11)$$

The polariton redshift caused by the cavity expansion is then

$$\Delta = E'_{\text{LPB}} - E_{\text{LPB}} = \frac{1}{2}[\delta - \sqrt{V_6^2 + (E_{c_2} + \delta - E_{P_6})^2} + \sqrt{V_6^2 + (E_{c_2} - E_{P_6})^2}]. \quad (12)$$

The experimental values of the polariton non-linearity in Figs. S4d,e are then corrected by removing an offset of  $\Delta$ , the results of which are presented in Figs. S4f,g. The slopes below 20 mW of the corrected data are fitted and plotted as the filled spherical symbols in Fig. S4j. Now, we see that the extrapolation of the corrected slopes in the AFM order towards highly photonic regime converges with the corrected slopes in the FM scenario at 0 meV/mW. For more excitonic regimes that are DC voltages  $>40$  V in FM order and  $>44$  V in AFM order, the compensation effect of cavity drift is nearly negligible. In low power regime, the LPB redshifts (blueshifts) in AFM (FM) order for all cavity detunings. In high power regime, the LPB has giant blueshifts for both magnetic orders and all cavity detuning scenarios.

#### Supplementary note 4: Exciton density estimation

The pump is a  $\lambda = 725$  nm laser that has a 200 fs pulse duration at a pulse-repetition frequency (PRF) of 76 MHz. The energy of a single pulse with  $P=1$  mW measured average power is

$$E_{\text{pulse}}^{1mW} = \frac{P}{PRF} = \frac{10^{-3} \text{ W}}{76 \times 10^6 \text{ Hz}} \simeq 1.316 \times 10^{-11} \text{ J} = 13.16 \text{ pJ}. \quad (13)$$

The energy of one photon is

$$E_{\text{photon}} = \frac{hc}{\lambda} \simeq 2.74 \times 10^{-19} \text{ J} = 2.74 \times 10^{-7} \text{ pJ}, \quad (14)$$

where  $h = 6.62607015 \times 10^{-34} \text{ J Hz}^{-1}$  and  $c = 2.99792458 \times 10^8 \text{ m Hz}$  are the Planck constant and vacuum light speed, respectively. The number of photons in a single pulse with average powers of 1 mW and 50 mW are

$$\begin{aligned} n_{\text{photon}}^{1mW} &= \frac{E_{\text{pulse}}^{1mW}}{E_{\text{photon}}} = 4.80 \times 10^7, \\ n_{\text{photon}}^{50mW} &= 2.40 \times 10^9. \end{aligned} \quad (15)$$

We utilize transfer matrix methods to simulate the open cavity structure (DBR/gap/CrSBr/DBR). Applying a cavity gap of 4025 nm yields polariton modes matching very well the PL spectrum in the AFM order and 44 V cavity detuning (Fig. S5a). The electric field intensity of 725 nm incidence is normalized for the simulations. Its amplitude drops to 0.009 in the CrSBr slab and 0.03 in the bottom DBR, signifying much stronger dielectric property of the CrSBr than the materials consisting of DBR (Fig. S5b). We subsequently quantify the absorption of the cavity system at 725 nm:  $A=1-R-T=0.0209$  (Fig. S5a). The exciton number for a 50 mW average excitation power is thus calculated as

$$n_X^{50mW} = A \cdot n_{\text{photon}}^{50mW} \simeq 5.02 \times 10^7. \quad (16)$$

We exclude the excitation scenarios by more than one laser pulses. The exciton reservoir depletes completely before the arrival of a following laser pulse because the exciton lifetime  $\sim 15 \text{ ps}^{44}$  in a CrSBr flake with similar thickness of 400 nm is three orders shorter than the pulse interval of 13.16 ns in our experiments. The polariton lifetime is supposed to be even shorter than the pure exciton scenario. Considering a layer thickness of  $0.8 \text{ nm}^{10,55}$ , our 312 nm

CrSBr flake contains  $m = 390$  layers. The excitation area on CrSBr  $S_X = \pi \cdot r^2 = 9\pi \mu\text{m}^2$  is referred from the burned regions in Fig. S1c. For an average pump power of 50 mW, the exciton density in each CrSBr layer is thus derived as

$$d_X^{50\text{mW}} = \frac{n_X^{50\text{mW}}}{m \cdot S_X} \simeq 4.53 \times 10^3 \mu\text{m}^{-2} = 4.54 \times 10^{11} \text{cm}^{-2} \quad (17)$$

Based on Eq. (11), we can rescale the exciton density of each layer for other pump powers (Fig. S5c). We can see that for this maximum pump power applied in our experiments, the exciton density in each CrSBr layer is well below the Mott density  $n_{\text{Mott}} \sim 10^{13} \text{cm}^{-2}$  in the transition metal dichalcogenide monolayers<sup>29,30</sup>. It is comparable to  $n_{\text{Mott}} \sim 10^{11} \text{cm}^{-2}$  in III-V<sup>56-58</sup> and II-VI<sup>59,60</sup> semiconductor quantum wells. However, due to the highly anisotropic reduced masses and dielectric properties, the excitonic wavefunction is quasi-1D along the b-axis with substantial charge density on the orbitals of Chromium and Sulfur<sup>31,32,61,62</sup>. The exciton radii along the a-axis<sup>31,33</sup> are on the same order of the unit cell scales<sup>32,63</sup>, so that the excitons in CrSBr can be regarded as mixed Frenkel and Wannier-Mott type<sup>31,33</sup>. This is in analogy to the single-wall carbon nanotubes where the excitons are 1D along the tube axis, and show both the Frenkel and Wannier-Mott characteristics<sup>64-67</sup>. The 1D confinement in hexagonal Boron Nitride (hBN) nanotubes also leads to Frenkel excitons<sup>68,69</sup> that can be distinguished from the Wannier-Mott excitons in the flat hBN<sup>70</sup>. In general, owing to the smaller exciton size, the Mott density of Frenkel excitons is supposed to be higher than their Wannier-Mott counterparts.

To be more quantitative, the effective exciton Bohr radius in CrSBr ( $a_B \sim 1.2 \text{ nm}$ )<sup>33</sup> is considerably smaller than those Wannier-Mott excitons ( $a_B \geq 4 \text{ nm}$ ) in conventional III-V and II-VI semiconductor systems<sup>71</sup>, so that in a rough estimation<sup>72</sup> the Mott density  $n_{\text{Mott}} \sim a_B^{-2}$  in CrSBr ought to be at least one order of magnitude higher than the  $10^{11}$  order. Therefore, We suppose that during the whole polariton nonlinearity measurements our system should not have experienced Mott transition where the electrons and holes are in a weak Coulomb-correlated plasma instead of the bound excitonic states<sup>73,74</sup>.

### Supplementary note 5: Theoretical model for exciton-magnon coupling

**Exciton** Here, we describe a theoretical model for excitons in CrSBr samples. We consider a system with bilayer configuration, as this allows to understand the overall behaviour in the presence of interlayer hybridization and spin ordering. The excitonic energy can be written as

$$E_X(\theta_1, \theta_2) = \varepsilon_g(\theta_1 - \theta_2) + E_b + \rho_X g_X, \quad (18)$$

where  $E_b$  is the exciton binding energy, and  $\varepsilon_g$  is the energy bandgap that accounts for corrections from magnetic ordering. This is described by angles  $\theta_1$  and  $\theta_2$  between the external magnetic field and the spin in layer 1 (upper) and layer 2 (lower). The bandgap of the material can be described as

$$\varepsilon_g(\theta_1 - \theta_2) = \varepsilon_0 + t \cos\left(\frac{\theta_1 - \theta_2}{2}\right), \quad (19)$$

including the dependence on the relative spin direction of the spin in upper and lower layer. This spin-dependent term originates from an overlap between interlayer spin wavefunctions. The overlap amplitude  $t$  is estimated to be 12 meV from our experiment (Fig. 1e). In the presence of background exciton with density  $\rho_X$ , this will lead to the non-linear shift of the exciton due to exciton-exciton exchange interaction.

To theoretically estimate  $g_X$ , we first model the exciton by the following creation field operator as

$$X_\sigma^\dagger = \sum_{\ell_c \ell_v} \sum_{\mathbf{k}} C_{\ell_c \ell_v}^\sigma \psi_\sigma^{\ell_c \ell_v}(\mathbf{k}) a_{\ell_c \mathbf{k} \sigma}^\dagger b_{\ell_v, -\mathbf{k} \sigma}, \quad (20)$$

where  $\psi_\sigma^{\ell_c \ell_v}(\mathbf{k})$  is the exciton wavefunction with  $\sigma$  and  $\mathbf{k}$  being the spin and in-plane crystal momentum. The layer



index for conduction band electron is  $\ell_c$  and for valence band hole  $\ell_v$ . As previously mentioned, we model our system by a bilayer CrSBr ( $\ell_c, \ell_v = 1, 2$ ), as this is the minimal case to investigate interlayer-intralayer hybridization effects. We note that including more layers into the theory will not change the result qualitatively.<sup>75</sup> With this, the intralayer exciton wavefunction are  $\psi_\sigma^{11}(\mathbf{k})$ ,  $\psi_\sigma^{22}(\mathbf{k})$  and the interlayer wavefunctions are  $\psi_\sigma^{12}(\mathbf{k})$ ,  $\psi_\sigma^{21}(\mathbf{k})$ . The interlayer and intralayer exciton hybridization coefficient is  $C_\sigma^{\ell\ell'}$ . The creation field operator of conduction band and the annihilation field operator of the valance band is  $a_{\mathbf{k}\sigma}^\dagger$  and  $b_{\mathbf{k}\sigma}$ .

The intralayer and interlayer excitonic states satisfy the Wannier equation

$$[\varepsilon_c(\mathbf{k}) - \varepsilon_v(\mathbf{k})]\psi_\sigma^{\ell_c\ell_v}(\mathbf{k}) - \sum_{\mathbf{q}} w_{\ell_c\ell_v}(\mathbf{q})\psi_\sigma(\mathbf{k} + \mathbf{q}) = E_\sigma^{\ell_c\ell_v}\psi_\sigma(\mathbf{k}), \quad (21)$$

where we adopted the Keldysh-like potential in the CrSBr bilayer. We consider the mass anisotropies in the dispersion

$$\varepsilon_c(\mathbf{k}) = \frac{k_x^2}{2m_{cx}} + \frac{k_y^2}{2m_{cy}}, \quad \varepsilon_v(\mathbf{k}) = -\frac{k_x^2}{2m_{vx}} - \frac{k_y^2}{2m_{vy}}. \quad (22)$$

The conduction band masses are  $m_{cx} = 7.31m_0$ ,  $m_{cy} = 0.14m_0$  and the valence band mass are  $m_{vx} = 2.84m_0$ ,  $m_{vy} = 0.45m_0$ <sup>31</sup>.

In CrSBr bilayer, we model the screened Coulomb interaction as<sup>76</sup>

$$v_{\ell\ell'}(\mathbf{q}) = \frac{2\pi}{\epsilon q} \frac{\kappa_{\ell\ell'}(q)}{(1 + r_*q)^2 - r_*^2q^2e^{-2qd}}, \quad (23)$$

where  $d = 7.93\text{\AA}$ <sup>77</sup> is the interlayer distance of the bilayer CrSBr  $\kappa_{12}(q) = \kappa_{21}(q) = e^{-qd}$  and  $\kappa_{11}(q) = \kappa_{22}(q) = 1 + r_*q(1 - e^{-2qd})$ . The screening length is<sup>75,78-80</sup>

$$r_* = \frac{\epsilon_s - 1}{\epsilon}d, \quad (24)$$

where  $\epsilon$  is the dielectric constant of the environment and  $\epsilon_s$  is the dielectric constant of CrSBr. Here, we let  $\epsilon_s \sim 6$  which gives binding energy  $E_\sigma^{11} = E_\sigma^{22} \approx 537$  meV in vacuum ( $\epsilon = 1$ ). In this calculation, we ignore the anisotropic screening for simplicity.

In anti-ferromagnetic (AFM) phase, interlayer tunneling is not allowed. However, in the ferromagnetic (FM) phase, the intralayer and interlayer excitons hybridized due to interlayer electrons tunneling. To account for the hybridization, we can solve for the coefficients  $C_\sigma^{\ell\ell'}$ <sup>81</sup> as

$$\begin{bmatrix} E_\sigma^{11} & -T_v & T_c & 0 \\ -T_v^* & E_\sigma^{12} & 0 & T_c \\ T_c^* & 0 & E_\sigma^{21} & -T_v \\ 0 & T_c^* & -T_v^* & E_\sigma^{22} \end{bmatrix} \begin{bmatrix} C_\sigma^{11} \\ C_\sigma^{12} \\ C_\sigma^{21} \\ C_\sigma^{22} \end{bmatrix} = E_b \begin{bmatrix} C_\sigma^{11} \\ C_\sigma^{12} \\ C_\sigma^{21} \\ C_\sigma^{22} \end{bmatrix}, \quad (25)$$

where the transition matrix elements are

$$T_v = t_v \sum_{\mathbf{k}} \bar{\psi}_\sigma^{11}(\mathbf{k})\psi_\sigma^{12}(\mathbf{k}), \quad T_c = t_c \sum_{\mathbf{k}} \bar{\psi}_\sigma^{11}(\mathbf{k})\psi_\sigma^{12}(\mathbf{k}). \quad (26)$$

Here, we consider the relevant valence band interlayer hopping  $t_v = t = 12$  meV and  $t_c = 0$ .<sup>31</sup>

In our analysis, we concentrate on  $1s$  states and set the total momentum of the exciton be  $\mathbf{Q} = 0$  in the scattering processes, such that we characterize the low-energy exciton-exciton (X-X) interactions with elastic scattering for  $\mathbf{Q} = 0$  only. The X-X interaction between exciton can be calculated from the total energy of the two-exciton state,

$\Omega_\sigma = \langle 0|X_\sigma X_\sigma \mathcal{H} X_\sigma^\dagger X_\sigma^\dagger|0\rangle = 2E_b + \Delta_\sigma$ . The interacting potential energy is given by

$$\Delta_\sigma = -2 \sum_{ss'} \sum_{\bar{s}\bar{s}'} \bar{C}_{s'}^\sigma \bar{C}_{\bar{s}'}^\sigma C_s^\sigma C_{\bar{s}}^\sigma V_{s\bar{s}}^{s'\bar{s}'}, \quad (27)$$

where  $s = (\ell_c, \ell_v)$  is the layer double index. The exchange interaction reads

$$V_{s\bar{s}}^{s'\bar{s}'} = \frac{1}{2A} \sum_{\mathbf{k}\bar{\mathbf{k}}\mathbf{q}} \sum_{\ell\ell'} f_{s\sigma}^\ell(\mathbf{k}, \mathbf{q}) w_{\ell\ell'}(\mathbf{q}) f_{\bar{s}\sigma}^{\ell'}(\mathbf{k}, -\mathbf{q}) \psi_{s'}^*(\mathbf{k}) \psi_{\bar{s}'}^*(\bar{\mathbf{k}}) \delta_{\ell_c\ell'_c} \delta_{\ell_v\ell'_v} \delta_{\ell_c\bar{\ell}'_c} \delta_{\ell_v\bar{\ell}'_v} \delta_{\mathbf{q}, \mathbf{k}-\bar{\mathbf{k}}}, \quad (28)$$

where  $A$  is the area of the sample. The above equation gives

$$g_X = A\Delta_\sigma. \quad (29)$$

We note that the direct interaction vanishes since we let the total momentum of the exciton  $Q = 0$ . Here,  $\mathbf{q}$  is the transferred momentum between excitons, with excitonic wavefunction being expressed in  $s$ -index notation as  $\psi_{s\sigma}(\mathbf{k}) = \psi_{\sigma}^{\ell_c\ell_v}(\mathbf{k})$ , and the factor  $f_{s\sigma}^\ell(\mathbf{k}, \mathbf{q}) = \delta_{\ell_c\ell} \psi_{s\sigma}(\mathbf{k}-\mathbf{q}) - \delta_{\ell_v\ell} \psi_{s\sigma}(\mathbf{k})$ . Using the wavefunction and  $t = 12 \text{ meV}$ , we find that the non-linearity is  $g_X \approx 0.29 \text{ } \mu\text{eV } \mu\text{m}^2$ . Interlayer hybridization only leads to a difference within  $0.01 \text{ } \mu\text{eV } \mu\text{m}^2$ .

Furthermore, the exciton-exciton interaction leads to a weak the non-linear blueshift which is not sufficient to account for the non-linear shift in the experiment, particularly the redshift in AFM phase. Even though this result is from a bilayer system, we do not expect our conclusions to change significantly in a system with large number of layers (bulk). Therefore, we consider additional contribution to non-linear energy shift from the coupling with magnon.

**Magnon** In this subsection, we investigate the non-linear energy shift due to exciton-magnon coupling. From Eq. S(18), the magnetic spin couple to the exciton through the bandgap term  $\varepsilon_g(\theta_1 - \theta_2)$ . In experiment, an out-of-plane magnetic field is applied to the sample (see Fig. S6). This points the spin at the equilibrium directions defined by  $\theta_{1*}$  and  $\theta_{2*}$ .

To obtain this equilibrium angles, we model the CrSBr as a bilayer spin system with energy density energy density (energy per unit cell) as

$$E_M = \frac{1}{N_s} \left[ \sum_{i=1}^{N_s} J \mathbf{S}_i^l \cdot \mathbf{S}_i^u - \sum_{i=1}^{N_s} \mu_0 (\mathbf{S}_i^l + \mathbf{S}_i^u) \cdot \mathbf{B} \right] \quad (30)$$

$$- \frac{1}{N_s} \sum_{i=1}^{N_s} \left( A_x S_{ix}^l S_{ix}^l + A_x S_{ix}^u S_{ix}^u \right) - \frac{1}{N_s} \sum_{i=1}^{N_s} \left( A_z S_{iz}^l S_{iz}^l + A_z S_{iz}^u S_{iz}^u \right) \quad (31)$$

where  $\mathbf{S}_i^{l,u}$  is the spin for lower and upper layer. The total number of unit cell is  $N_s$ . The interlayer magnetic exchange coupling  $J = 24.8 \text{ } \mu\text{eV}$  and the anisotropic exchange to the easy axis is  $A_x = 72.5 \text{ } \mu\text{eV}$  and to the out-of-plane axis is  $A_z = 14.4 \text{ } \mu\text{eV}$ ,<sup>82</sup> where we set the hard axis anisotropic exchanged be zero. The last term is the magnetic anisotropy that gives the preferential direction of the spin in  $x$ -direction (we remind that CrSBr is a quasi-1D system). Here, we note that the interlayer exchange interaction  $J$  has a similar strength as the anisotropy  $A_x$ . As a function of orientation angles the energy can be written as

$$E_M(\theta_1, \theta_2) = JS^2 \cos(\theta_1 - \theta_2) - \mu_0 SB(\cos \theta_1 + \cos \theta_2) - A_x S^2 (\sin^2 \theta_1 + \sin^2 \theta_2) - A_z S^2 (\cos^2 \theta_1 + \cos^2 \theta_2), \quad (32)$$

where  $S = 3/2$  is the spin at chromium site. The angle between the upper (lower) layer spin and the magnetic field is defined as  $\theta_1$  ( $\theta_2$ ).

To find the tilted angle with the applied magnetic field  $B$ , we minimize the total energy by solving

$$\left. \frac{\partial E_M}{\partial \theta_1} \right|_{\theta_{1*}, \theta_{2*}} = 0, \quad \left. \frac{\partial E_M}{\partial \theta_2} \right|_{\theta_{1*}, \theta_{2*}} = 0. \quad (33)$$

Assuming that  $\theta_1 = \theta_{1*}$  and  $\theta_2 = \theta_{2*}$  admit minimum solution of  $E_M$ , this leads to

$$\frac{\partial E_M}{\partial \theta_1} = -JS^2 \sin(\theta_{1*} - \theta_{2*}) + \mu_0 SB \sin \theta_{1*} - (A_x - A_z)S^2 \sin 2\theta_{1*} = 0, \quad (34)$$

$$\frac{\partial E_M}{\partial \theta_2} = JS^2 \sin(\theta_{1*} - \theta_{2*}) + \mu_0 SB \sin \theta_{2*} - (A_x - A_z)S^2 \sin 2\theta_{2*} = 0. \quad (35)$$

Solving the above equations, we obtain the solution that minimizes  $E_M$ . The saturation field  $B_{\text{sat}}$  can be obtained using Eqs. (34) and (35),

$$B = \frac{2JS \sin(\theta_{1*} - \theta_{2*}) + (A_x - A_z)S(\sin 2\theta_{1*} - \sin 2\theta_{2*})}{\mu_0(\sin \theta_{1*} - \sin \theta_{2*})} \quad (36)$$

by taking the limits  $\theta_1, \theta_2 \rightarrow 0$ . This gives the saturation magnetic field

$$B_{\text{sat}} = 2S \frac{(J + A_x - A_z)}{\mu_0} \quad (37)$$

in the ferromagnetic phase.

The spins in CrSBr are dynamic and can fluctuate around the equilibrium directions with small angle  $\delta_1$  and  $\delta_2$  (see Figure S6). We expand the energy in the vicinity of this point as

$$E_M(\theta_{1*} + \delta_1, \theta_{2*} + \delta_2) \approx E_M(\theta_{1*}, \theta_{2*}) + a\delta_1^2 + 2b\delta_1\delta_2 + c\delta_2^2, \quad (38)$$

where

$$\begin{aligned} a &= \frac{\partial^2 E_M(\theta_{1*}, \theta_{2*})}{\partial \theta_{*1}^2} = -JS^2 \cos(\theta_{1*} - \theta_{2*}) + \mu_0 SB \cos \theta_{1*} - 2(A_x - A_z)S^2 \cos 2\theta_{1*}, \\ b &= \frac{\partial^2 E_M(\theta_{1*}, \theta_{2*})}{\partial \theta_{*1} \partial \theta_{*2}} = JS^2 \cos(\theta_{1*} - \theta_{2*}), \\ c &= \frac{\partial^2 E_M(\theta_{1*}, \theta_{2*})}{\partial \theta_{*2}^2} = -JS^2 \cos(\theta_{1*} - \theta_{2*}) + \mu_0 SB \cos \theta_{2*} - 2(A_x - A_z)S^2 \cos 2\theta_{2*}. \end{aligned}$$

We write Eq. (38) in to the magnon normal modes as

$$E_M(\theta_{1*} + \delta_1, \theta_{2*} + \delta_2) \approx E_M(\theta_{1*}, \theta_{2*}) + \omega_- \eta_-^2 + \omega_+ \eta_+^2, \quad (39)$$

where the normal mode frequencies  $\omega_+$  and  $\omega_-$  are the eigenvalue of the matrix,

$$\omega_{\pm} = \frac{(a + c) \pm \sqrt{(a - c)^2 + 4b^2}}{2}, \quad (40)$$

and the normal eigenmodes are

$$\eta_{\pm} = \frac{(\omega_{\pm} - c)}{\sqrt{b^2 + (\omega_{\pm} - c)^2}} \delta_1 + \frac{b}{\sqrt{b^2 + (\omega_{\pm} - c)^2}} \delta_2. \quad (41)$$

Therefore, the change of the bandgap as

$$\varepsilon_g(\theta_{1*} + \delta_1, \theta_{2*} + \delta_2) = \varepsilon_0 - t \left[ \cos^2 \frac{1}{2} \theta_* - \sin \theta_* (\beta_+ \eta_+ - \beta_- \eta_-) - \cos \theta_* (\beta_+ \eta_+ - \beta_- \eta_-)^2 \right] \quad (42)$$

with

$$\beta_+ = \frac{(1 + (\omega_- - c)/b)\alpha_+}{\omega_+ - \omega_-}, \quad \beta_- = \frac{(1 + (\omega_+ - c)/b)\alpha_-}{\omega_+ - \omega_-} \quad (43)$$

The magnon-exciton coupling is zero at AFM ( $\theta_{1*} = -\theta_{2*} = \pi/2$ ) and FM ( $\theta_{1*} = \theta_{2*} = 0$ ) phase. This implies there is no redshift in this phase if we disregard the fluctuation of the quadratic terms.

**Thermal effect and incoherent magnon** In nonzero finite temperature, we measure the average exciton energy in Eq. (18) due to the thermal fluctuation of the spins.<sup>6</sup>

$$\bar{E}_X(\theta_{1*}, \theta_{2*}) = \bar{\varepsilon}_g(\theta_{1*} - \theta_{2*}) + E_b + \rho_X g_X, \quad (44)$$

where the average is

$$\bar{\varepsilon}_g(\theta_{1*} - \theta_{2*}) = \varepsilon_0 - t \left[ \cos^2 \frac{1}{2} \theta_* - \sin \theta_* (\beta_+ \langle \eta_+ \rangle - \beta_- \langle \eta_- \rangle) - \cos \theta_* (\beta_+^2 \langle \eta_+^2 \rangle - 2\beta_+ \beta_- \langle \eta_+ \eta_- \rangle + \beta_-^2 \langle \eta_-^2 \rangle) \right]. \quad (45)$$

The small fluctuation around  $\theta_*$ , denoted as  $\eta_{\pm}$ , can take positive and negative. Therefore, we may expect  $\langle \eta_{\pm} \rangle = 0$  and disregard the linear coupling term (second term). However, in the last term, we expect  $\langle \eta_{\pm}^2 \rangle \propto n_{\pm}$  where  $n_{\pm}$  is the total number of the ( $\pm$ ) magnons modes in the sample.  $\eta_{\pm}^2$  is proportional to the amplitude square. For the the cross-term, we have  $\langle \eta_+ \eta_- \rangle = \langle \eta_+ \rangle \langle \eta_- \rangle = 0$ , since  $\eta_+$  and  $\eta_-$  are two independent orthogonal modes. This reduces the measure bandgap to

$$\bar{\varepsilon}_g(\theta_{1*}, \theta_{2*}) = \varepsilon_0 - t \left[ \cos^2 \frac{1}{2} \theta_* - \cos \theta_* (\beta_+^2 \langle \eta_+^2 \rangle + \beta_-^2 \langle \eta_-^2 \rangle) \right] \quad (46)$$

To calculate the  $\langle \eta_{\pm}^2 \rangle$ , we model the thermal effects using canonical ensemble with the partition function as

$$Z = \int_{-\eta_+^c}^{\eta_+^c} d\eta_+ \int_{-\eta_-^c}^{\eta_-^c} d\eta_- e^{-\frac{1}{k_B T} [E_M(\theta_{1*}, \theta_{2*}) + \omega_- \eta_-^2 + \omega_+ \eta_+^2]} = e^{-\frac{1}{k_B T} E_M(\theta_{1*}, \theta_{2*})} \prod_{i=\pm} \sqrt{\frac{\pi k_B T}{\omega_i}} \operatorname{erf} \left( \eta_i^c \sqrt{\frac{\omega_i}{k_B T}} \right), \quad (47)$$

where  $\eta_{\pm}^c$  is the cutoff that are related to the maximum fluctuation in  $\delta_1$  and  $\delta_2$ . Therefore, this gives

$$\begin{aligned} \langle \eta_{\pm}^2 \rangle &= \frac{1}{Z} \int_{-\eta_{\pm}^c}^{\eta_{\pm}^c} d\eta_{\pm} \int_{-\eta_{\mp}^c}^{\eta_{\mp}^c} d\eta_{\mp} \eta_{\pm}^2 e^{-\frac{1}{k_B T} [E_M(\theta_{1*}, \theta_{2*}) + \omega_- \eta_-^2 + \omega_+ \eta_+^2]} \\ &= \left( \frac{k_B T}{2\omega_{\pm}} \operatorname{erf} \left( \eta_{\pm}^c \sqrt{\frac{\omega_{\pm}}{k_B T}} \right) - \frac{\eta_{\pm}^c}{\sqrt{\pi}} e^{-\frac{(\eta_{\pm}^c)^2}{k_B T}} \right) / \operatorname{erf} \left( \eta_{\pm}^c \sqrt{\frac{\omega_{\pm}}{k_B T}} \right) \end{aligned} \quad (48)$$

In the low-temperature  $\omega_{\pm}/k_B T \rightarrow \infty$ . This gives the following simple result,

$$\langle \eta_{\pm}^2 \rangle = \frac{1}{2} k_B T / \omega_{\pm}. \quad (49)$$

Here, the temperature  $T$  is the magnonic temperature which is proportional to the pump intensity. This result can also be understood intuitively by considering the total number of thermally-excited magnon, since the  $k_B T$  is the thermal energy and  $\omega_{\pm}$  is a single magnon energy.

Note that the result in Eq. (49) holds only for the case of magnon energy being sufficiently large. However, for the cases where the magnon energy is small we can no longer take  $\omega_{\pm}/k_B T \rightarrow \infty$ . In the case we take a limit  $\omega_{\pm} \rightarrow 0$  in Eq.(48), leading to

$$\langle \eta_{\pm}^2 \rangle \approx \frac{(\eta_{\pm}^c)^2}{3}. \quad (50)$$

In this case, almost every available low-energy magnons get excited.

Therefore, we arrive at the exciton energy written as

$$\bar{E}_X(\theta_{1*}, \theta_{2*}) = \varepsilon_0 - t \left[ \cos^2 \frac{1}{2}(\theta_{1*} - \theta_{2*}) - \left( \beta_+^2 \langle \eta_+^2 \rangle + \beta_-^2 \langle \eta_-^2 \rangle \right) \cos(\theta_{1*} - \theta_{2*}) \right] + E_b + \rho_X g_X \quad (51)$$

where  $\varepsilon_g(\theta_{1*} - \theta_{2*})$  is the bandgap,  $E_b$  is the exciton binding energy, and  $g_X$  is the exciton-exciton exchange interacting strength. Using Eqs. (40), (41), and (43), we obtain the important result for explaining the findings in different magnetic configurations:

$$\bar{E}_X(\pi/2, -\pi/2) = \varepsilon_0 - t \frac{k_B T}{\omega_-} + E_b + \rho_X g_X, \quad (\text{AFM}) \quad (52)$$

$$\bar{E}_X(0, 0) = \varepsilon_0 - t + t \frac{2}{3} (\eta_-^c)^2 + E_b + \rho_X g_X, \quad (\text{FM}) \quad (53)$$

where in the FM phase the magnon energy near  $B = B_{\text{sat}}$  is very small. As  $B > B_{\text{sat}}$ , the incoherent magnon ( $\eta_-$ -mode) shift in FM phase take the general form in Eq. S(48).

To investigate the polaritonic response in CrSBr, we recognize that the created exciton is hybridized with the intrinsic cavity mode forming a self-hybridize polariton in strong light-matter coupling regime. We model this self-hybridized polariton as follows:

$$\mathcal{H}_p = \begin{bmatrix} \omega_c & \Omega \\ \Omega & \bar{E}_X(\theta_{1*}, \theta_{2*}) \end{bmatrix}, \quad (54)$$

where  $\omega_c$  is the intrinsic cavity mode with  $\omega_c \approx \varepsilon_0 + E_b$ . The Rabi splitting  $\Omega$  also experiences a non-linear response due to phase space filling effect.<sup>35</sup> The lower polariton in this system has the energy

$$\mathcal{E} = \frac{1}{2} [\omega_c + E_X(\theta_{1*}, \theta_{2*})] - \sqrt{\frac{1}{2} [\omega_c - E_X(\theta_{1*}, \theta_{2*})]^2 + \Omega^2} \quad (55)$$

In the above, we may approximate the Rabi splitting as  $\Omega = \Omega_0 \left( 1 - \frac{1}{2} \frac{a_X^2 \rho_X}{(1+\gamma_c)(1+\gamma_v)} \right)$ ,<sup>35</sup> where  $\gamma_{c/v} = m_{c/v}/(m_c + m_v)(a_X/\sqrt{A})$  with  $m_{c/v} = \sqrt{m_{c/v,x} m_{c/v,y}}$  being the geometrical average of the conduction/valence band masses and  $a_X = \langle r \rangle$  being the average distance of the between the electron and the hole (exciton size) from theoretical estimation is

$$a_X = \begin{cases} 1.0 \text{ nm} & \text{AFM, intralayer exciton,} \\ 1.1 \text{ nm} & \text{FM, hybridized exciton.} \end{cases} \quad (56)$$

Also, the Rabi splitting in low-density regime is  $\Omega_0 \approx 0.24 \text{ eV}$ .<sup>6</sup> We write the energy shift due to the small change in temperature  $\Delta T$  and exciton density  $\Delta \rho_X$  by expanding it as

$$\Delta \mathcal{E} = \mathcal{B} \Delta T + \mathcal{A} \Delta \rho_X, \quad (57)$$

where

$$\mathcal{B} = \left[ \frac{1}{2} + \frac{\omega_c - \bar{E}_X^{(0)}}{2\Lambda} \right] \frac{\partial \bar{E}_X}{\partial T}, \quad (58)$$

$$\mathcal{A} = \left( \frac{1}{2} + \frac{\omega_c - \bar{E}_X^{(0)}}{2\Lambda} \right) \frac{\partial \bar{E}_X}{\partial \rho_X} - \frac{\Omega_0}{2\Lambda} \frac{\partial \Omega}{\partial \rho_X}. \quad (59)$$

Here, we have defined  $\Lambda = \sqrt{\frac{1}{2}(\omega_c - E_X^{(0)})^2 + \Omega_0^2}$  with  $E_X^{(0)} = \varepsilon_0 - t \cos^2 \frac{1}{2}(\theta_{1*} - \theta_{2*}) + E_b$ . The derivatives are

$$\frac{\partial \bar{E}_X}{\partial T} = \left( \beta_+^2 \frac{\partial \langle \eta_+^2 \rangle}{\partial T} + \beta_-^2 \frac{\partial \langle \eta_-^2 \rangle}{\partial T} \right) \cos \frac{1}{2}(\theta_{1*} - \theta_{2*}), \quad (60)$$

$$\frac{\partial \bar{E}_X}{\partial \rho_X} = g_X, \quad (61)$$

$$\frac{\partial \Omega}{\partial \rho_X} = - \frac{\Omega_0 a_X^2 / 2}{(1 + \gamma_c^2)(1 + \gamma_v^2)}. \quad (62)$$

Assuming  $\gamma_{c,v} \approx 0$ , we find the saturation factor  $\frac{\partial \Omega}{\partial \rho_X} \approx -0.24 \mu\text{eV}\mu\text{m}^2$  which is as large as  $g_X$  and it is another important nonlinear effect. The energy shift due to laser power is

$$\Delta \mathcal{E}_{\text{AFM}} = - \left[ \frac{1}{2} + \frac{\omega_c - \bar{E}_X^{(0)}}{2\Lambda} \right] \frac{tk_B}{\omega_-} \Delta T + \left[ \left( \frac{1}{2} + \frac{\omega_c - \bar{E}_X^{(0)}}{2\Lambda} \right) g_X + \frac{\Omega_0}{2\Lambda} \frac{a_X^2 / 2}{(1 + \gamma_c^2)(1 + \gamma_v^2)} \right] \Delta \rho_X, \quad (\text{AFM}) \quad (63)$$

$$\Delta \mathcal{E}_{\text{FM}} = \left[ \left( \frac{1}{2} + \frac{\omega_c - \bar{E}_X^{(0)}}{2\Lambda} \right) g_X + \frac{\Omega_0}{2\Lambda} \frac{a_X^2 / 2}{(1 + \gamma_c^2)(1 + \gamma_v^2)} \right] \Delta \rho_X, \quad (\text{FM}) \quad (64)$$

where the magnon energy  $\omega_- = S^2(J + A_x - A_z)$  with the magnetic exchange couplings  $J = 24.8 \mu\text{eV}$ ,  $A_x = 72.5 \mu\text{eV}$  and  $A_z = 14.4 \mu\text{eV}$ .<sup>82</sup>

In the FM phase, since the magnon energy is very small, almost all the available magnonic excited states are depleted immediately with small temperature change. This results in the very low temperature-dependent blueshift. Therefore, in this case, the exciton energy nonlinear blueshift is mostly coming from the exciton-exciton exchange interaction. This is consistent to the non-linear response that we observed in high-power measurement. We found the maximum blue shift (Fig. 2h) is  $\Delta \mathcal{E} = 2.3 \text{ meV}$ .

As we can see, the magnon fluctuating term in AFM phase is negative leading to the redshift. Moreover, we find this effect rather strong. Changing the temperature by  $\Delta T \approx 1.6 \text{ K}$  is sufficient to generate a  $\Delta \mathcal{E}_{\text{FM}} = -2 \text{ meV}$  redshift in exciton energy if we assume the maximum blueshift coming from the saturation and exciton-exciton interaction is  $\Delta \mathcal{E}_{\text{FM}} = 2.3 \text{ meV}$ . Furthermore, we have let  $\omega_c - E_X^{(0)} \approx 0$  (small detuning). Therefore, it is very likely the blueshift coming from exciton-exciton interaction is compensated, leading to the overall redshift.

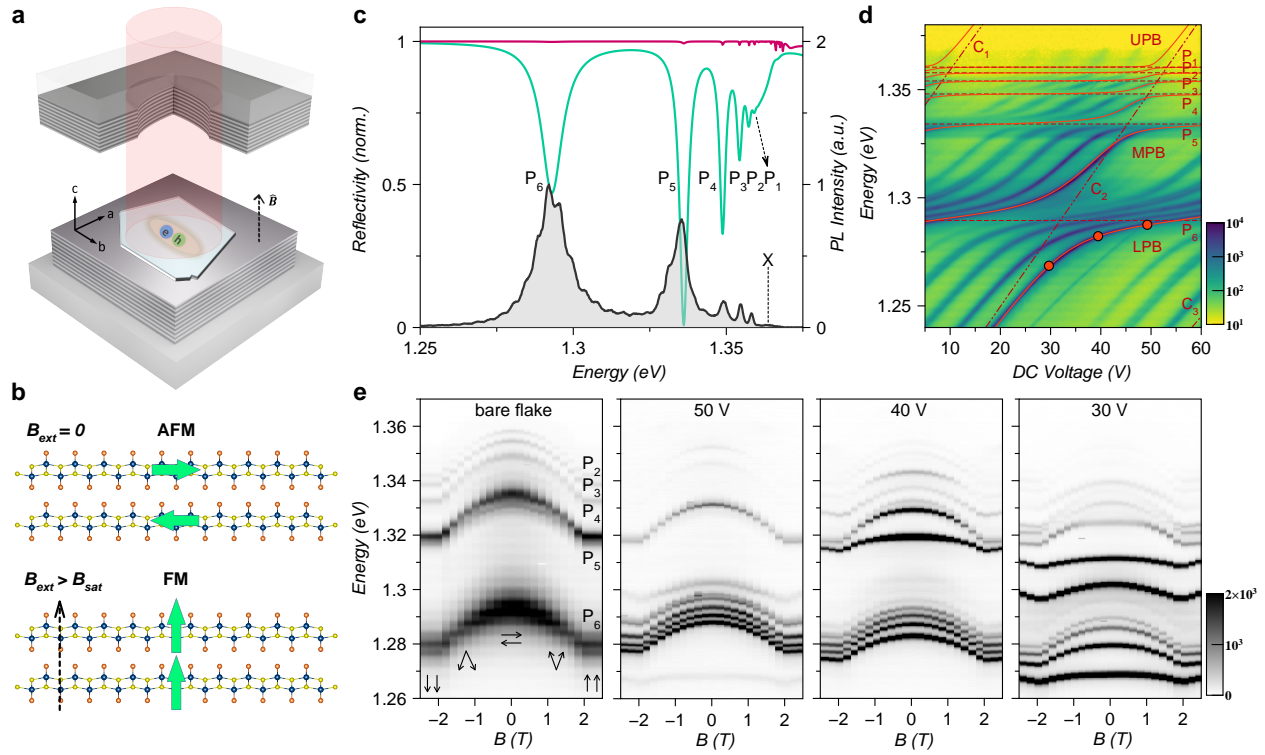
### Supplementary note 6: Correlation measurements of the polariton condensates in FM order

Figure S8a shows a schematics of the Michelson interferometer for measuring the first-order correlation of polariton condensate. As an example, the cartoon of mesa is used to demonstrate the spatial inversion of the images reflected from two arms. In our measurements, the reflected beam from the reference arm is aligned to transmit through the center of the last focusing lens. The reflected beam from the delay arm is parallel to that of the reference arm, but has a spatial displacement. Both images are focused and overlapped on the detector. More detailed operations of this interferometer can be found in the Methods section of the manuscript.

Figure S8b shows the power dependent interference pattern (upper panels) as well as the calculated first-order correla-

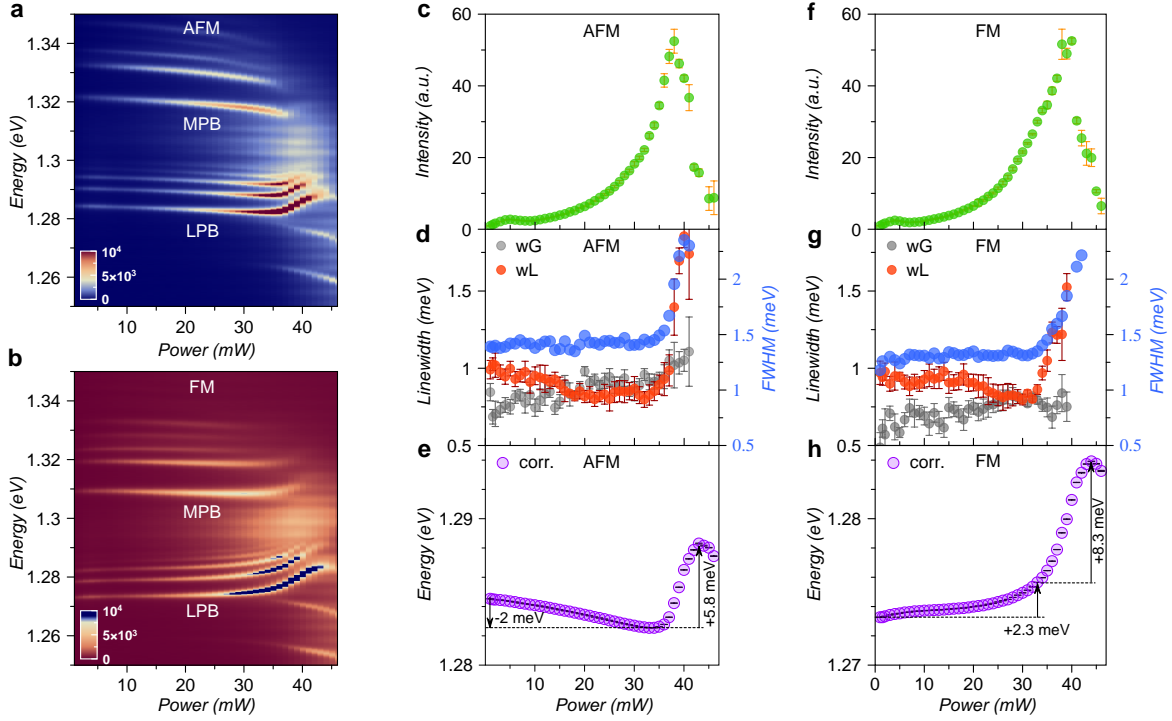
tion function (lower panels) of the LPB in FM order of sample position 2 (cavity detuning voltage of 38 V and external magnetic field of 3 T). Its PL spectrum at a minimum pump power is shown in Fig. S4c. The excitation condition of the power dependence is the same as in Fig. 3a of the manuscript. We can see that the maximum interference visibility as well as the first-order correlation function  $g^{(1)}(\vec{r}, 0)$  is obtained at an averaged pump power around 29 mW, and then both of them decrease at higher pump powers, corresponding to the same turning point of the coherence length decrease shown in Fig. 3c of the manuscript.

Figure S9 show the complete power dependent second-order correlation measurements of the LPBs in AFM and FM orders in Fig. S4c. we can see that in both magnetic orders the  $g^{(2)}(0)$  decreases with increasing pump power, signifying the coherence build-up of the polaritons which is consistent with the 1st-order coherence measurements in Supplementary Fig. S8b and Fig. 3a of the manuscript. The power-dependent  $g^{(2)}(0)$  values are summarized in Fig. 3c of the manuscript.



**Fig. 1 | Exciton-polaritons of CrSBr in an external tunable microcavity.** **a.** Schematics of the cryogenic open optical microcavity. The excitons have optical dipoles aligned to the in-plane crystallographic  $b$ -axis. **b.** Schematics of the magnetic orders in CrSBr. The green arrows indicate the orientation of layer net magnetization. Top panel: anti-ferromagnetic (AFM) ground state below the Néel temperature. Bottom panel: forced ferromagnetic (FM) order in presence of an out-of-plane saturation field  $B_{\text{sat}} \sim 2$  T. **c.** PL measurement (black) and reflectivity of a 318 nm thick CrSBr flake on the DBR simulated by transfer matrix method with (green) and without (magenta) excitonic absorption. Six self-hybridized polariton states ( $P_1$ - $P_6$ ) are observed in PL measurements. The exciton resonance of 1.3655 eV is used for the reflection simulation, matching perfectly with the PL spectrum. **d.** PL measurements with different cavity detunings (DC voltages). Red lines are the fitting of the polariton modes (solid), self-hybridized polaritons (dashed), and the cavity modes (dotted-dashed). The energies of the self-hybridized polaritons used in the fitting and the coupling strengths are summarized in Supplementary Table. S1. **e.** Magneto-PL of the polariton modes in bare flake and the external cavity with different cavity detuning scenarios marked by the red dots in **d**. The spin canting regime by an out-of-plane magnetic field is illustrated in the left panel.





**Fig. 2 | Magnetically tunable exciton-polariton non-linearity.** **a.** Pump power dependent PL spectra of polaritons with a detuning voltage of 44 V at 0 T (AFM order). **b.** Pump power dependent PL spectra of polaritons with a detuning voltage of 38 V at 3 T (FM order). **c.** Intensity, **d.** linewidths, and **e.** energy of the lowest LPB mode in the AFM ordered phase. **f.** Intensity, **g.** linewidths, and **h.** energy of the lowest LPB mode in the FM ordered phase. The Voigt fitting function yields the Gaussian (grey) and Lorentzian (red) linewidths as well as the full-width at half maxima (FWHM, blue). The experimentally measured polariton energy shifts (hollow dots in Supplementary Figs. S4d,e) are corrected by removing the redshift due to the thermal expansion of the cavity with increasing pump power.

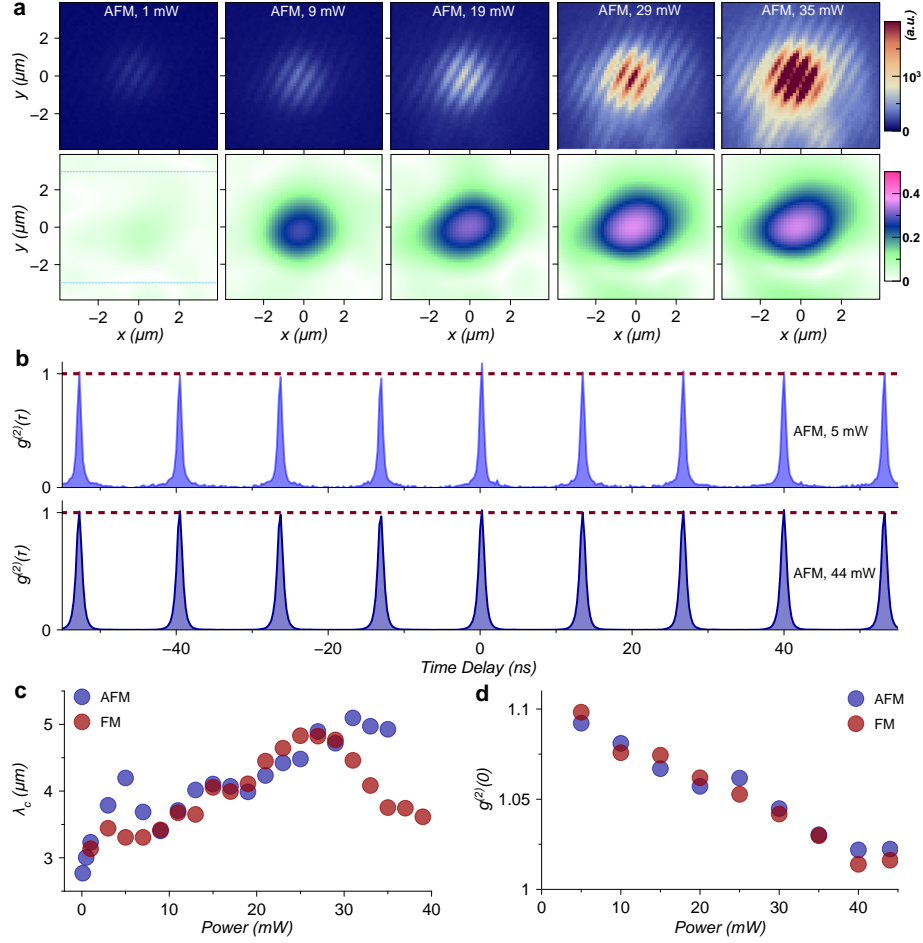
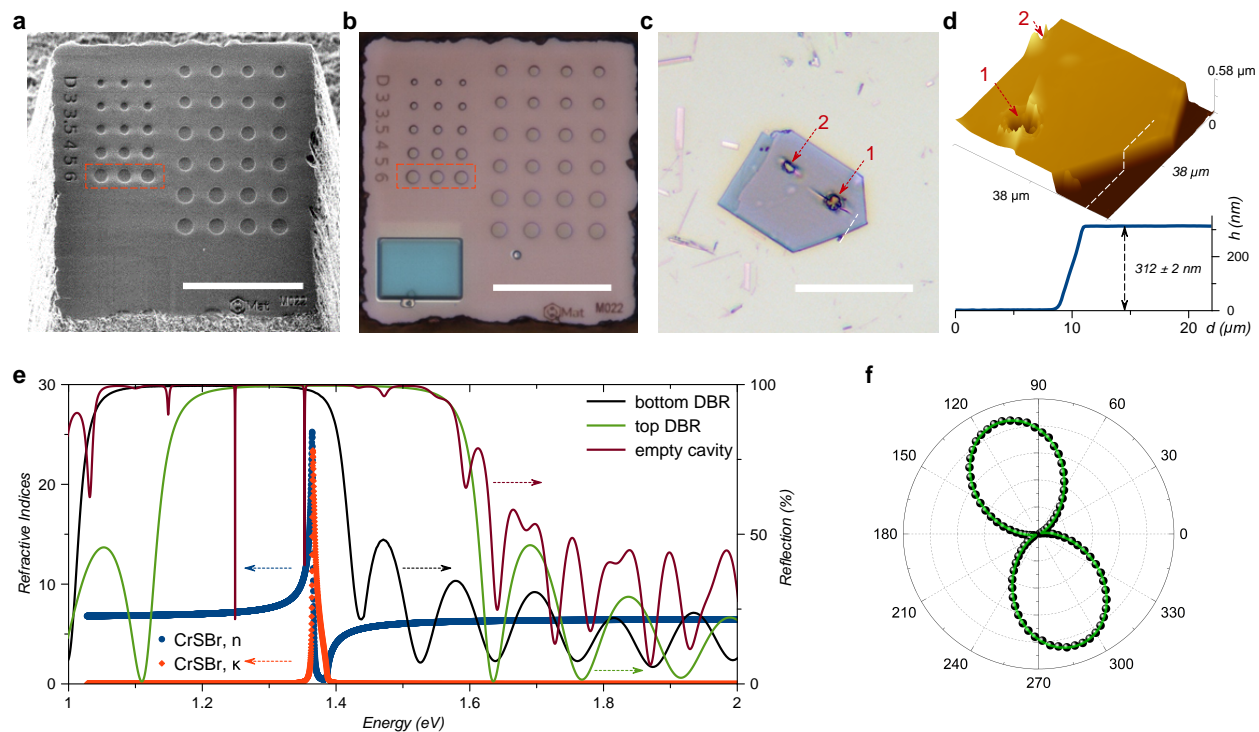
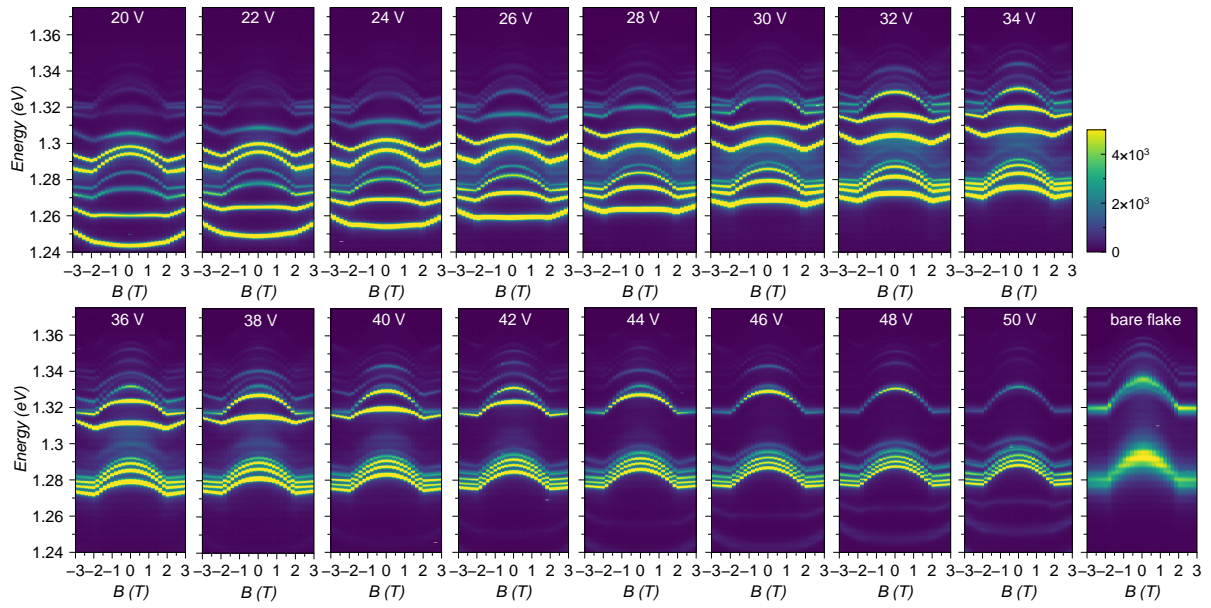


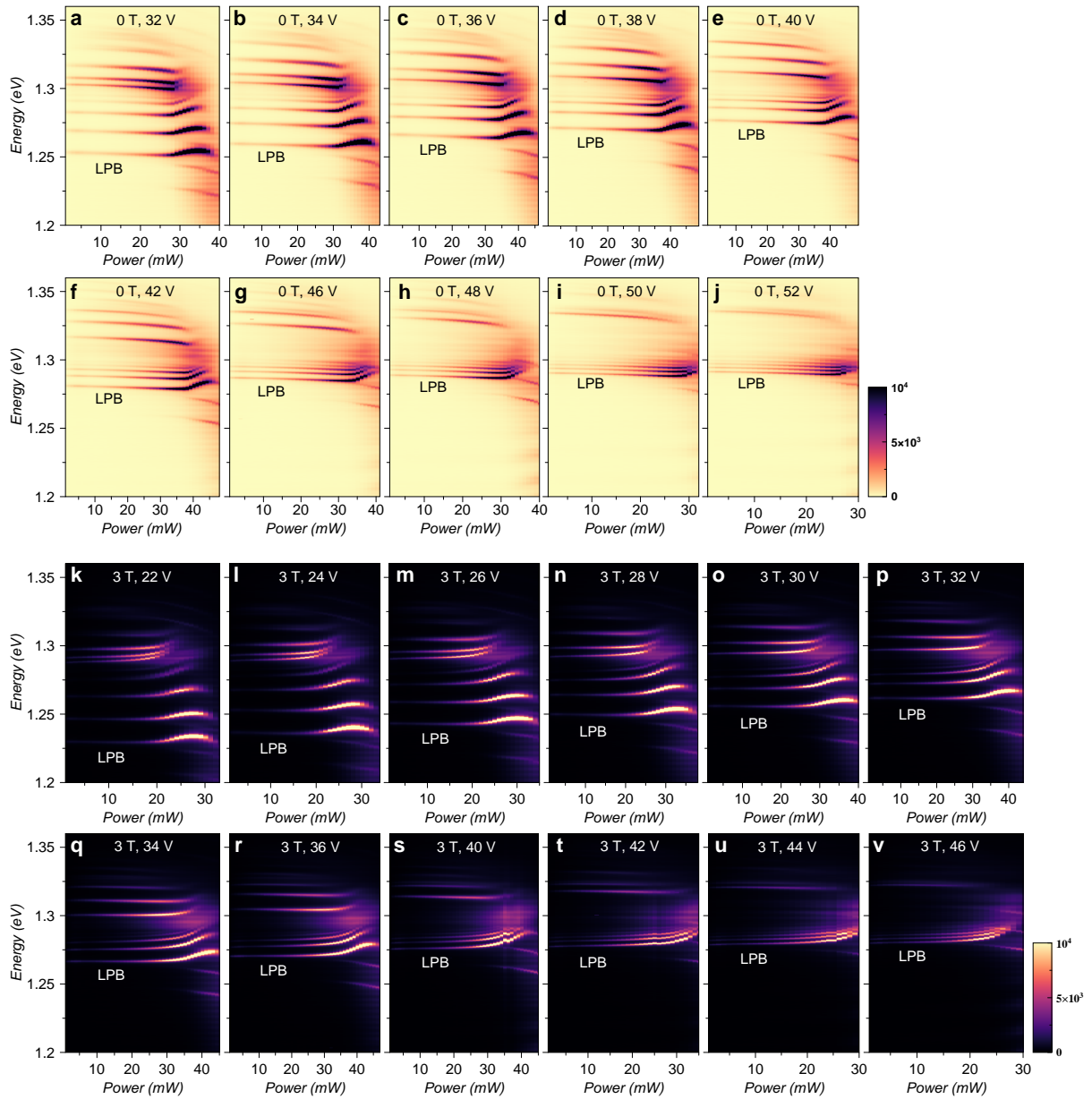
**Fig. 3 | Correlation measurements of the exciton-polariton condensate.** **a.** Upper panels: power dependence of the zero-delay spatial interference of the LPB analysed in Fig. 2a. Lower panels: spatially-resolved first-order correlation function  $g^{(1)}(\vec{r}, 0)$  at pump powers corresponding to the upper panels. The two dashed lines in the bottom left graph show a  $6 \mu\text{m}$  confined region for vertical binning of  $g^{(1)}(\vec{r}, 0)$ , which is then fitted by a Gaussian function to extract the FWHM ' $x_c$ ' in the horizontal direction. **b.** Second-order correlation measurements of the LPB analysed in Fig. 2a at representative pump powers of 5 mW and 44 mW. The dashed flat lines mark the Poisson level (unity). **c.** Coherence length derived by using  $\lambda_c = \sqrt{\pi} x_c$ , and **d.** Power dependent second-order auto-correlation  $g^{(2)}(0)$  of the LPB in AFM and FM orders. The first- and second-order correlation measurements for the LPB in FM order of Fig. 2b can be found in Supplementary Figs. S8 and S9, respectively.



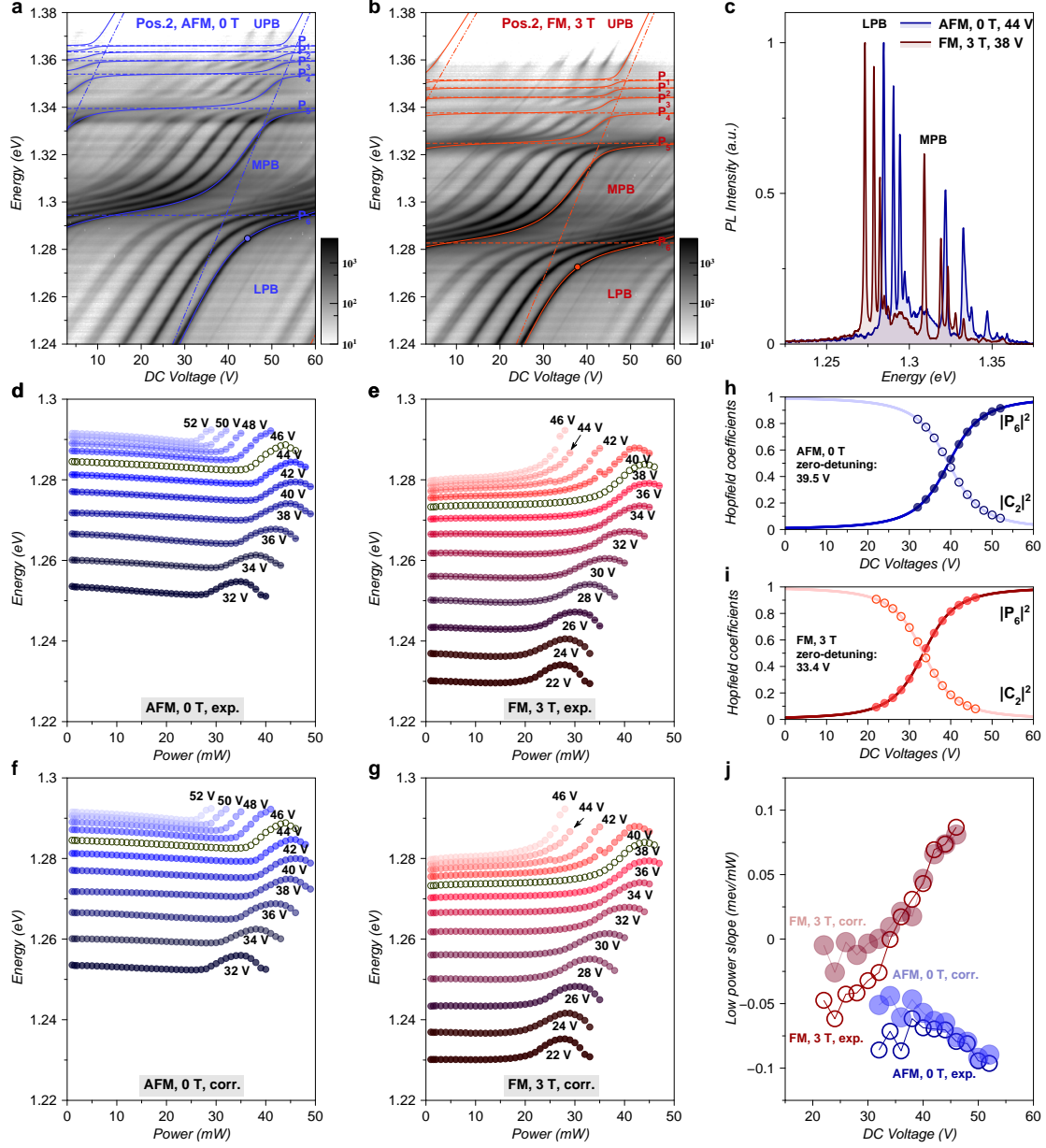
**Supplementary Fig. S1 | Cavity and material properties.** **a.** Scanning electron microscope image of the mesa after FIB etching. The  $6 \mu\text{m}$  lens pits are marked by the red frame. **b.** Optical microscope of the mesa after sputtering with DBR. The  $6 \mu\text{m}$  lenses (concave DBR) are marked by the red frame. **c.** Microscope image of the CrSBr flake transferred on the bottom DBR. The scale bars in **a-c** are all  $50 \mu\text{m}$ . The holes (1:  $6 \mu\text{m} \times 4 \mu\text{m}$ ; 2:  $4 \mu\text{m} \times 5 \mu\text{m}$ ) are burned through the  $6 \mu\text{m}$  lenses by 725 nm femtosecond laser with high power ( $0.92 \text{ nJ/pulse}$ ). **d.** Upper panel: atomic force microscopy of the CrSBr flake in **c**. Lower panel: step profile along the white dashed lines in the upper panel and **c**. The measured thickness ( $h = 312 \pm 2$  nm) matches perfectly with the simulation by the transfer matrix in Fig. 1c of the manuscript. **e.** Reflection of the top and bottom DBR, and empty cavity with a gap of 4025 nm, simulated by the transfer matrix method, and the complex refractive index  $\tilde{n} = n + i\kappa$  of CrSBr used for the transfer matrix simulation in Fig. 1c of the manuscript. **f.** Polarization dependent PL emission intensity (black dots) of the LPB at 20 V detuning voltage in Fig. 1d of the manuscript. The fit (green) determines the crystallographic b-axis as  $110^\circ$  or  $290^\circ$  in our experimental geometry.



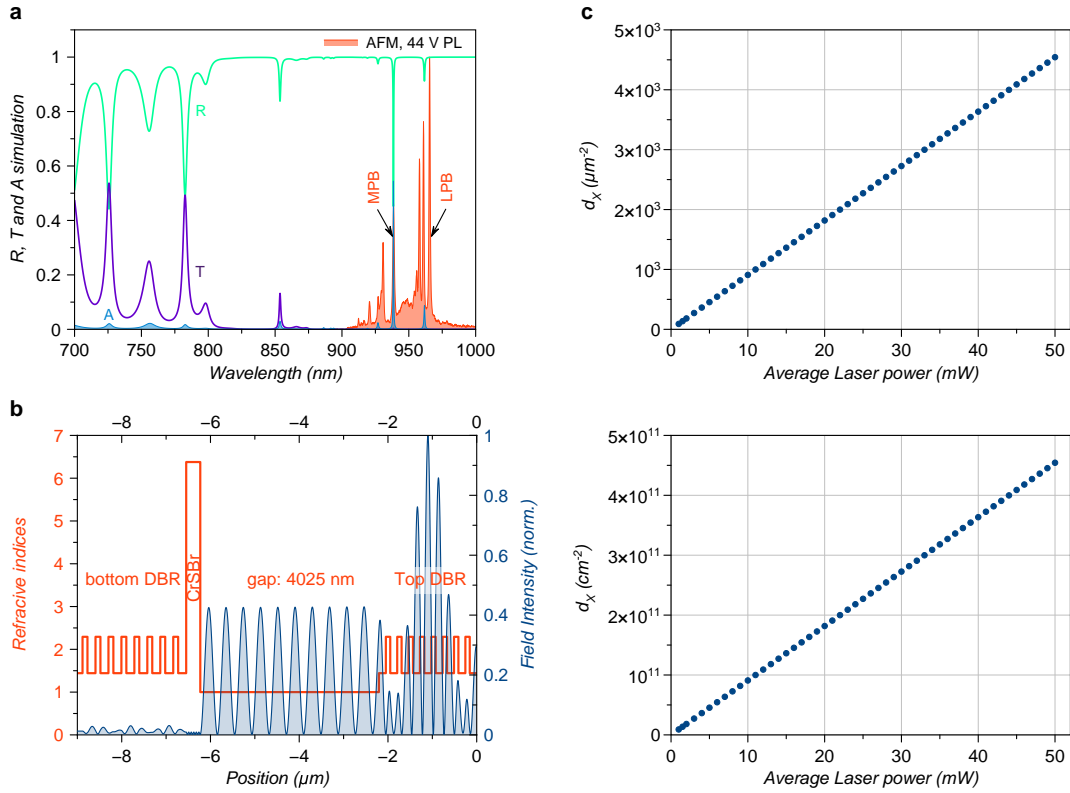
**Supplementary Fig. S2| Magneto-PL of sample position 1 at different cavity detunings.** The measurements are performed between  $\pm 3$  T for detuning DC voltages from 20 V to 50 V. All graphs share the same colorbar. The cavity length gets smaller and the modes blueshift for saturation magnetic fields  $|B| \geq 2$  T. The drifts for magnetic field intensity  $|B| < 2$  T is less than 1 meV.



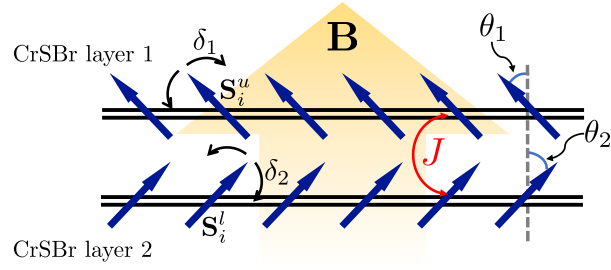
**Supplementary Fig. S3 | Pump power dependent PL measurements of sample position 2.** **a-j.** cavity detuning voltages of 32-52 V and AFM order (0 T). **k-v.** cavity detuning voltages of 22-46 V and FM order (3 T). The two colorbars apply to measurements with different magnetic orders. The voltages in **a-j** and **k-v** correspond to those in cavity detuning PL measurements in Fig. S4a and Fig. S4b, respectively. The power dependent PL measurements at 44 V (0 T) and 38 V (3 T) detuning voltages are shown in Fig. 2a and Fig. 2b in the manuscript, respectively.



**Supplementary Fig. S4 LPB non-linearity with different cavity detunings and magnetic orders.** PL measurements of sample position 2 as a function of cavity detunings (DC voltages) in **a**. AFM order (0 T) and **b**. FM order (3 T). The experiments are performed with a pump power of 0.5 mW, far below the condensate thresholds. Additionally plotted lines are the fitting of the polariton modes (solid), self-hybridized polaritons (dashed), and the cavity modes (dotted-dashed), resulting from a  $9 \times 9$  coupled oscillators model. **c**. PL spectra at detuning voltages of 44 V of the AFM order and 38 V of the FM order that are marked by the dots in **a** and **b**. These two detuning voltages correspond to the same detuning energy relative to the  $P_6$  self-hybridized polariton, where the polariton non-linearity in Fig. 2 of the manuscript is measured. Detuning dependent LPB energy shifts with increasing pump power in **d**. AFM order (0 T) and **e**. FM order (3 T), fitted from the data in Fig. S2. Corrected LPB energy shifts with increasing pump in **f**. AFM order (0 T) and **g**. FM order (3 T). **h**. AFM order (0 T), and **i**. FM order (3 T) Hopfield coefficients (the ratios of  $P_6$  self-hybridized polariton:  $|P_6|$  and the external cavity mode:  $|C_2|$ ) of the LPBs with different detunings, which are calculated by a  $2 \times 2$  coupled oscillator model in Eqs. S8-S11. The dots and circles mark the detunings where polariton non-linearities are measured in **d-g** and Fig. S2. **j**. The experimental (empty symbols) and corrected (filled symbols) slopes of the LPB energy shifts below 20 mW in **d-g**, fitted by a linear function.

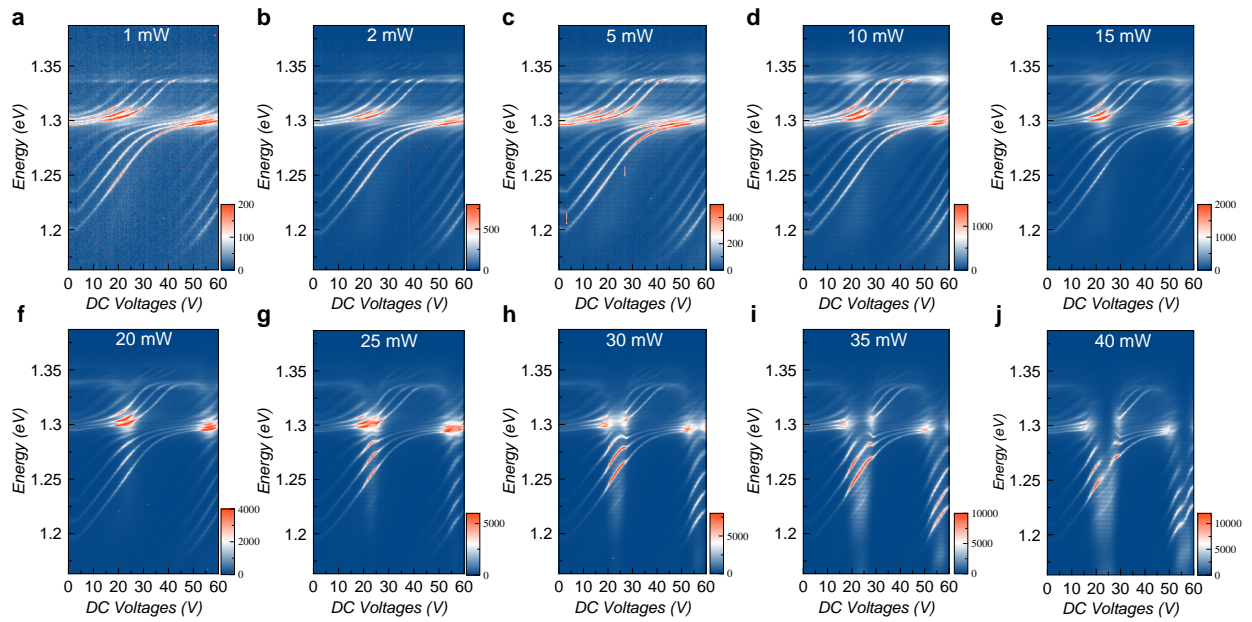


**Supplementary Fig. S5 | Simulation of full cavity structure.** **a.** Simulated reflection (R), transmission (T), and absorption (A) of 965 nm light in the open cavity with a gap of 4025 nm by transfer matrix method. The PL spectrum (AFM order, 44 V) matches very well the simulations. There is a few nanometers discrepancy of the LPB, probably due to the admixture of the unknown photonic tunneling. The absorption at 725 nm is 0.0209. **b.** The electric field intensity distribution in the cavity and corresponding structure of the dielectric layers of the cavity. **c.** Conversion between exciton density in each layer and the average pump power. Top (bottom) panel: unit in  $\mu\text{m}^{-2}$  ( $\text{cm}^{-2}$ ).

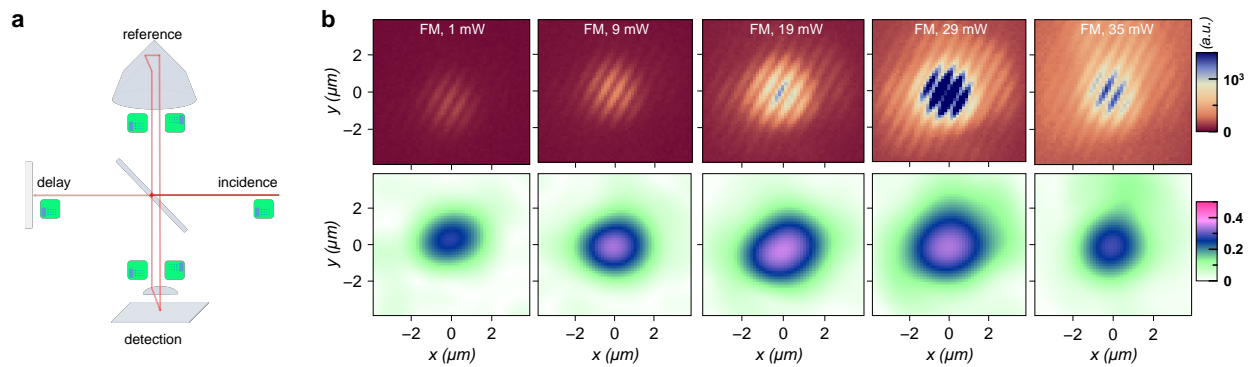


**Supplementary Fig. S6 | Schematic diagram for the spin model in bilayer CrSBr.** The spin in the upper and lower layer at site  $i$  are  $\mathbf{S}_i^u$  and  $\mathbf{S}_i^l$ . Their interlayer spin exchange coupling is  $J$ . In the presence of the uniform out-of-plane magnetic field  $\mathbf{B}$ , the spins  $\mathbf{S}_i^u$  ( $\mathbf{S}_i^l$ ) become tilted, forming an angle  $\theta_1$  ( $\theta_2$ ) with respect to  $\mathbf{B}$ -field. In non-zero temperature, the spins  $\mathbf{S}_i^u$  ( $\mathbf{S}_i^l$ ) fluctuate around its equilibrium orientation with small angle  $\delta_1$  ( $\delta_2$ ).

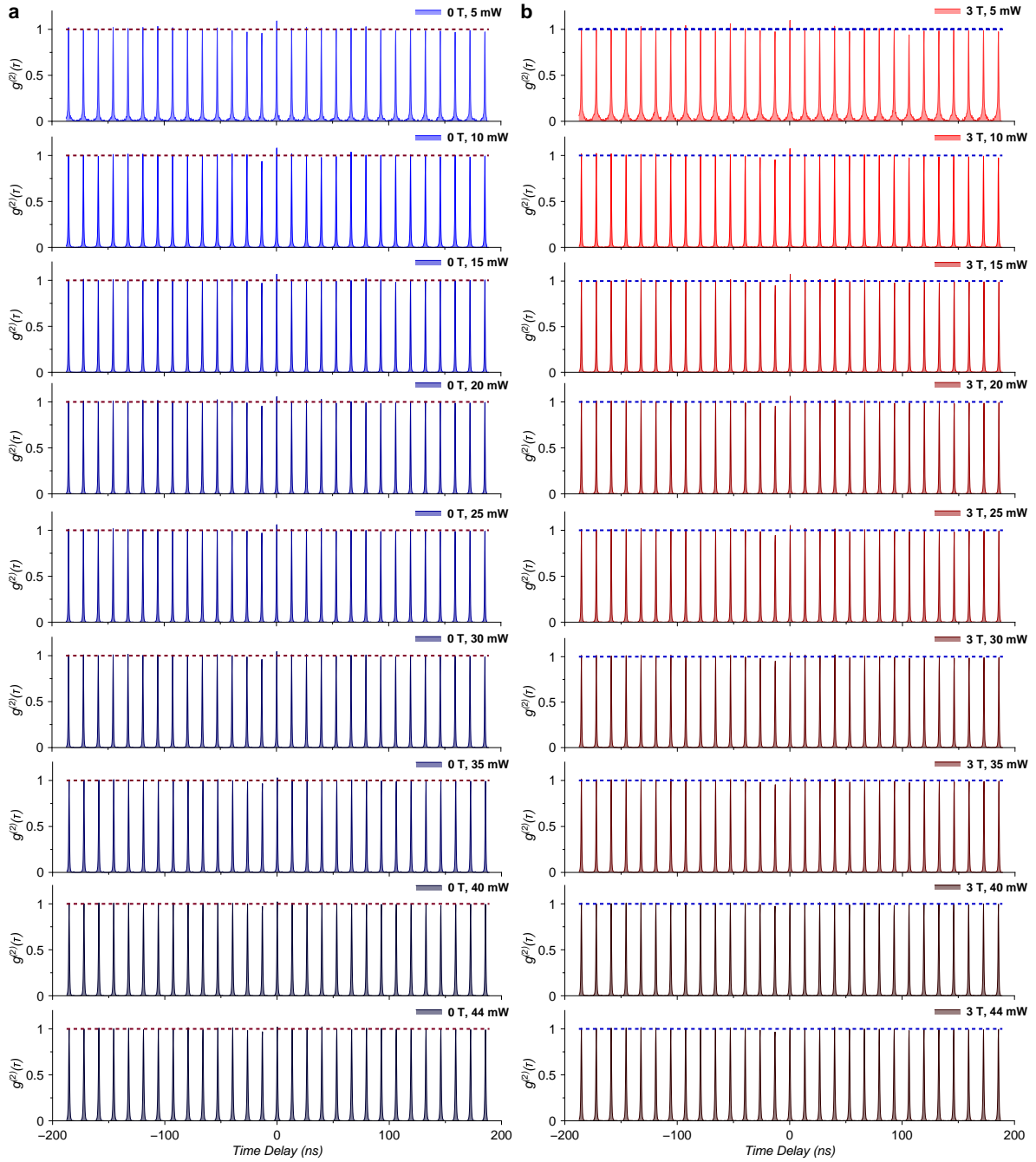




**Supplementary Fig. S7 | Power dependent PL of cavity detuning on sample position 2 (AFM, 0 T).** The threshold phenomenon is clear around 20 mW pump power. The stimulated polaritonic scattering is then more obvious for higher powers, leading to the condensation into the lowest polariton modes (for cavity detuning around 22 V and 55 V of two consecutive longitudinal mode sets). At maximum power of 40 mW, the Rabi gap collapses and the system reaches the optical saturation.



**Supplementary Fig. S8 | First-order correlation of the exciton-polariton condensate at 3 T. a.** Schematics of the Michelson interferometer. The sample image as well as the real-space emission patterns from the reference arm is spatially inverted. **b.** Top panels: Pump power dependent zero-delay interference patterns of the FM order (3 T, 38 V detuning) LPB emission in Fig. S4c. Bottom panels: calculated spatially-resolved first-order correlation  $g^{(1)}(\vec{r}, 0)$  at the pump powers corresponding to the upper panels.



**Supplementary Fig. S9 | Second-order correlation of the exciton-polariton condensate. a.** Pump power dependent  $g^{(2)}(\tau)$  of the LPB emission in AFM order (0 T, 44 V) of Supplementary Fig. S4c. **b.** Pump power dependent  $g^{(2)}(\tau)$  of the LPB emission in FM order (3 T, 38 V) of Supplementary Fig. S4c.